10
Smart textile composites integrated with fibre optic sensors

XIAOMING TAO

10.1   Introduction

The rapid development in textile structural composites (TSCs) has created new marketing and research opportunities for the textile industry and textile scientists.[1] According to their structural integrity, three-dimensional textile composites have a network of yarn bundles in an integrated manner, thereby giving rise to significant increases in inter- and intralaminar strength, higher feasibility of complex structural shape formation, and greater possibility of large-scale manufacturing at reduced cost as compared with traditional laminated composites. Their higher strength and stiffness with lighter weight have led to increasing applications in aerospace, automobile industries and civil engineering. It has been predicted that the improvement of TSC fabrication technologies and their combination with smart structure technologies will lead to major industrial growth in the next century by challenging the position of metals and other conventional engineering materials.

A success in developing TSC fabrication technology relies on a better understanding of the processing structure–properties relationship. An important step in this direction involves the monitoring of the internal strain/stress distributions in realtime during the fabrication of textile preforms and the subsequent solidification to their final structures. Another important issue in the application of TSCs is to make them sensitive to their internal health conditions and external environments. Integration of sensing networks inside fabric-reinforced structures is considered to be the first step to make the materials smart. Furthermore, the complexity of the TSC structure, for instance, the skin–core effect of three-dimensional braid composites, makes characterization of the material a very difficult task. In the past, it has been almost impossible to measure the internal stress/strain distribution of such a complex material by using conventional methods such as strain gauges and ultrasonic sensors. In addition, there is a need for some kind of sensing network embedded in the structures to offer a means to (1) monitor the

internal stress distribution of TSCs *in situ* during the manufacturing process, (2) allow health monitoring and damage assessment of TSCs during services, and (3) enable a control system to actively monitor and react to the changes in the working environment.

Fibre optic technologies offering both sensing and signal transmission functions have attracted considerable attention in recent years, especially in smart concrete structures including highways, bridges, dams and buildings.[2,3] A number of researchers have applied fibre optic sensor (FOS) technologies to manufacture process monitoring and structure health assessment for fibre-reinforced composites.[4–6] Since optical fibres are of small size and lightweight, compatible with textile yarns, and readily embedded or even woven inside TSCs, they are the most promising medium to form the sensing network mentioned above.

This chapter provides a review of various types of fibre optic sensors, major issues of smart textile composites integrated with fibre Bragg grating sensors, that is temperature and strain coupling, sensitivity, multiaxial strain measurement, measurement effectiveness and reliability issues, as well as various measurement systems for smart textile composites integrated with fibre optic sensors.

10.2   Optical fibres and fibre optic sensors

Normally, an optical fibre consists of a core surrounded by a cladding whose refractive index is slightly smaller than that of the core. The optic fibre is coated during the fibre drawing process with a protective layer of polymer. Inside the fibre core, light rays incident on the core-cladding boundary at angles greater than the critical angle undergo total internal reflection and are guided through the core without refraction. Silica glass is the most common material for optical fibres, where the cladding is normally made from pure fused silica, and the core from doped silica containing a few mol% of germanium. Other dopants, such as phosphorus, can also be used. Extra-low absorption occurs in a germanosilicate fibre with a local minimum attenuation coefficient $\alpha = 0.3\,dB/km$ at 1.3 µm and an absolute minimum $\alpha = 0.16\,dB/km$ at 1.55 µm. Therefore, light in the two windows travels down tens of kilometres of fibre without strong attenuation in a correct guided mode condition. This is why optical fibre has been replacing copper coaxial cable as the preferred transmission medium for electromagnetic waves, revolutionizing the world's communication today.

Parallel with the rapid development in the area of optical fibre communications, fibre optical sensors have also attracted much attention and experienced a fast growth in the recent years. They are lightweight, small and flexible; thus they will not affect the structure integrity of the composite materials and can

be integrated with the reinforcing fabrics to form the backbones in structures. They are based on a single common technology that enables devices to be developed for sensing numerous physical perturbations of a mechanical, acoustic, electric, magnetic and thermal nature. A number of sensors can be multiplexed along a single optical fibre using wavelength-, frequency-, time- and polarization-division techniques to form one-, two- or three-dimensional distributed sensing systems. They do not provide a conducting path through the structure and do not generate additional heat that could potentially damage the structure. They do not require electrical isolation from the structural material and do not generate electromagnetic interference; this could be a crucial advantage in some applications.

For the applications in smart structures, FOSs can be divided according to whether sensing is distributed, localized (point) or multiplexed (multipoint).[6] If sensing is distributed along the length of the fibre, the measurand distribution as a function of position can be determined from the output signal, so a single fibre can effectively monitor the changes in the entire object into which it is embedded. A localized sensor detects measurand variation only in the vicinity of the sensor. Some localized sensors can lead themselves to multiplexing, in which multiple localised sensors are placed at intervals along the fibre length. Each sensor can be isolated by wavelength, time or frequency discrimination, thereby allowing the real-time profiling of parameters throughout the structure.

Before the invention of fibre Bragg gratings (FBGs), FOSs could be classified into two broad categories, intensiometric and interferometric, according to the sensing scheme. Intensiometric sensors are simply based on the amount of light detected through the fibre. In its simplest form, a stoppage of transmission due to breakage of a fibre embedded in the structure indicates possible damage. Interferometric sensors have been developed for a range of high-sensitivity applications, such as acoustic and magnetic field sensors, and are usually based on single-mode fibres. For example, the Mach–Zehnder interferometer, as shown in Fig. 10.1, is one of the most common configurations. With this type of device, strain can be monitored directly by embedding the sensing fibre arm in the structure, while the referencing arm of equal length is isolated from the environment. Although such a configuration is highly sensitive to strain, the whole fibre length in the signal arm responds to strain, and thus localization of the sensing region is difficult. An alternative interferometric sensor, more suitable for localized sensing, is based on interference between light reflected from two closely spaced surfaces, which form a short gauge length Fabry–Perot (FP)-type interferometer (Fig. 10.2). The strain or stress applied on the gauge inside the structure can be determined by measuring the reflected spectrum or reflected light signal from the FP cavity, which is a function of the distance between the two reflected surfaces. The disadvantage of such devices is that it is difficult to perform
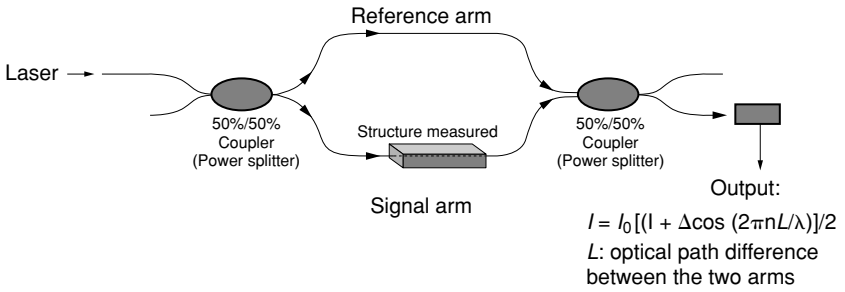
10.1 Measurement by interferometric sensors with Mach–Zehnder interferometer.
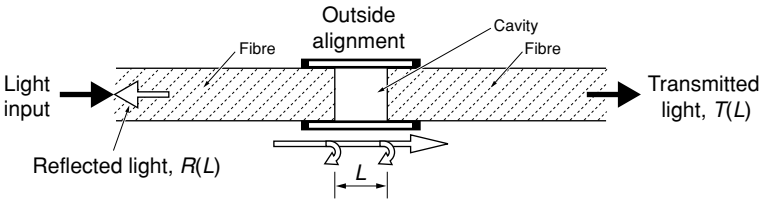
10.2 Measurement by interferometric sensors with Fabry–Perot-type interferometer.

absolute measurements, and hard to form a multiplexing sensor array along a single fibre length due to the large loss of the discontinuing structure of an FP cavity. Detailed review and analysis have been given by Udd[7] and Measures.[8]

10.3   Principal analysis of embedded fibre Bragg grating sensors

10.3.1 Principle of FBGS

As FBGs have many advantages over the other two groups, and show great promise, we will concentrate on FBGs in this section. The FBG is fabricated by modulation of the refractive index of the core in a single mode optic fibre, which has been described in detail in Chapters 8 and 9. Assume that the change in the index modulation period is independent of the state of polarization of the interrogating light and only dependent on the fibre axial strain, differentiating the Bragg wavelength in Eq. (9.15) yields:

$$\frac{\Delta\lambda}{\lambda} = \varepsilon_1 + \frac{\Delta n}{n} \qquad [10.1]$$

where ε_1 is the total axial strain of the optic fibre. Generally speaking, λ and n will have different values in the directions of polarization. Subscript $i = 1, 2, 3$ is denoted for λ and n as their values in the defined polarized direction. A local

Cartesian coordinate system is used, with 1, 2, 3 representing the three principal directions respectively. Eq. (10.1) can be rewritten as:

$$\frac{\Delta\lambda_i}{\lambda_i} = \varepsilon_1 + \frac{\Delta n_i}{n_i}$$ [10.2]

For strain, subscript ($j = 1, 2, 3, 4, 5, 6$) is used. The first three represent the normal strains in the first (fibre axis), second, third directions, respectively, the latter three being the three shear strains, respectively. The strain ε of an optic fibre may be contributed by either thermal expansion or stress, hence the symbol ε^* is used for the optic fibre strain induced by stress only. The refraction index n is related to both temperature T and strain ε^*, therefore:

$$\frac{\Delta n_i}{n_i} = \frac{1}{n_i}\sum_j \frac{\partial n_i}{\partial \varepsilon_j^*}\varepsilon_j^* + \frac{\partial n_i}{\partial T}\Delta T$$ [10.3]

According to the strain optic theory:[9]

$$\frac{1}{n_i}\sum_j \frac{\partial n_i}{\partial \varepsilon_j^*}\varepsilon_j^* = -\frac{n_i^2}{2}\sum_j P_{ij}\varepsilon_j^*$$ [10.4]

where P_{ij} is the strain-optic coefficient matrix. For a homogeneous isotropic medium,

$$P_{ij} = \begin{bmatrix} P_{11} & P_{12} & P_{12} & & & \\ P_{12} & P_{11} & P_{12} & & 0 & \\ P_{12} & P_{12} & P_{11} & & & \\ & & & P_{44} & & \\ & 0 & & & P_{44} & \\ & & & & & P_{44} \end{bmatrix}$$ [10.5]

where $P_{44} = (P_{11} - P_{12})/2$.

For a homogeneous isotropic medium, it can be assumed that the index of refraction n has a linear relation with temperature T:

$$\xi = \frac{\partial n_i}{\partial T}$$ [10.6]

where ξ is regarded as a thermo-optic constant.

Because lights are transverse waves, only the transverse (2, 3 directions) deviations of the reflective index can cause the shift of the Bragg wavelength. Substituting Eqs. (10.4), (10.5) and (10.6) into Eq. (10.3), the peak wavelength shifts for the light linearly polarized in the second and third directions are given below:

$$\frac{\Delta\lambda_2}{\lambda_2} = \varepsilon_1 - \frac{n_2^2}{2}[P_{11}\varepsilon_2^* + P_{12}(\varepsilon_1^* + \varepsilon_3^*)] + \xi\Delta T \qquad [10.7]$$

and

$$\frac{\Delta\lambda_3}{\lambda_3} = \varepsilon_1 - \frac{n_3^2}{2}[P_{11}\varepsilon_3^* + P_{12}(\varepsilon_1^* + \varepsilon_2^*)] + \xi\Delta T \qquad [10.8]$$

In many cases, the wavelength shift for the Bragg grating sensor observed for each polarization eigen-mode of the optical fibre depends on all the three principal strain components within the optical fibre. Sirkis and Haslach[10] extended Butter and Hocker's model[9] and have shown that their results are closer to those observed in transverse loading experiments[11] for the interferometric optical fibre sensor.

The general cases will be discussed in Section 10.4.2. Here we will only discuss the axisymmetric problem where $\varepsilon_2^* = \varepsilon_3^*$. If the optic fibre is a thermal isotropic material with a constant expansion coefficient α, then $\varepsilon_j^* = \varepsilon_j - \alpha\Delta T$ ($j = 1, 2, 3$). Eqs. (10.7), (10.8) can be written into the same form:

$$\frac{\Delta\lambda}{\lambda} = \varepsilon_1\left\{1 - \frac{n^2}{2}\left[P_{12} + (P_{11} + P_{12})\frac{\varepsilon_2}{\varepsilon_1}\right]\right\}$$
$$+ \alpha\frac{n^2}{2}(P_{11} + 2P_{12})\Delta T + \xi\Delta T$$
$$= f\varepsilon_1 + \xi^*\Delta T \qquad [10.9]$$

where

$$f = 1 - \frac{n^2}{2}\left[P_{12} + (P_{11} + P_{12})\frac{\varepsilon_2}{\varepsilon_1}\right] \qquad [10.10]$$

and

$$\xi^* = \xi + \frac{\alpha n^2}{2}(P_{11} + 2P_{12}) \qquad [10.11]$$

f is defined as the sensitivity factor, ξ^* as the revised optic-thermal constant.
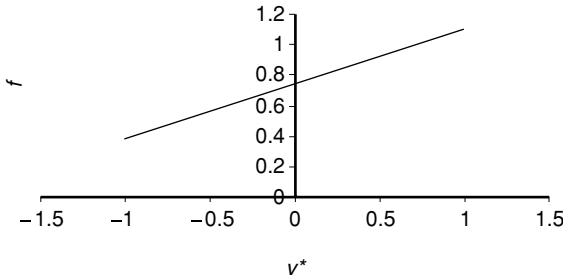
10.3.2 Sensitivity factor

10.3.2.1 Axial strain measurement alone

When the temperature change is so small that its effect can be ignored, the FBG can be considered as a strain sensor. Let us define $\upsilon^* = (-\varepsilon_2/\varepsilon_1)$ as the effective Poisson's ratio (EPR) of optic fibre. From Eq. (10.11), it is obvious that the sensitivity factor f is not a constant but a function of υ^*,

Table 10.1 Material parameters of single mode silica optic fibres

Strain-optic coefficient		Index of refraction (n)	Elastic modulus E (GPa)	Poisson's ratio v
P_{11}	P_{12}			
0.113	0.252	1.458	70	0.17

10.3 Sensitivity factor plotted against effective Poisson's ratio.

$$f = 1 - \frac{n^2}{2}[P_{12} - (P_{11} + P_{12})v^*]$$ [10.12]

Figure 10.3 shows a typical curve of the sensitivity factor as a function of the effective Poisson's ratio, calculated by using the material parameters of optic fibre, provided in Table 10.1.

Let us consider the following special cases:

1. $v^* = 0.17$, $f = 0.798$: which implies that the EPR is equal to the fibre material Poisson's ratio and meets the requirement of Butter and Hocker's assumption.[9] The value of sensitivity factor, $f = 0.798$, is recommended by many FBGS manufacturers;

2. $v^* = -1$, $f = 0.344$: which implies that the strains in three principal directions of the fibre are equal, which corresponds to the case of static uniform stress or the case of thermal expansion;

3. $v^* = 0.0$, $f = 0.732$; which implies that there is no transverse deformation.

Therefore, if an FBGS is used as an embedded sensor, it is necessary to make a correction of the sensitivity factor with respect to the transverse principal strain. Otherwise, only when the transverse principal strain of the optic fibre is not sensitive to the host's strain field can the sensitivity factor be regarded as a constant.

10.3.2.2 Temperature measurement alone

If a stand-alone FBGS is subjected to a temperature change, then:

$$\varepsilon_1 = \varepsilon_2 = \alpha \Delta T$$

where α is the isothermal expansion coefficient of the optic fibre. Substituting the above equation into Eq. (10.9), we can derive the following:

$$\frac{\Delta\lambda}{\lambda} = \left\{ \alpha \left[1 - \frac{n^2}{2}(2P_{12} + P_{11}) \right] + \xi^* \right\} \Delta T = (\alpha + \xi)\Delta T$$

Usually ξ is over ten times greater than α (for silica, $\alpha = 0.55 \times 10^{-6}$, $\xi = 8.3 \times 10^{-6}$), therefore the effect of thermal expansion on the measurement result may be negligible for such a stand-alone FBGS.

10.3.3 Temperature and strain coupling

As an embedded strain sensor, ideally, the measured strain ε_1 in Eq. (10.9) should represent the host strain in the optic fibre direction. The temperature compensation can be made simply by:

$$\varepsilon_1 = (\Delta\lambda/\lambda - \xi^*\Delta T)/f \qquad [10.13]$$

For the germanium-doped silica core,[8] the thermal-optic coefficient ξ is approximately equal to 8.3×10^{-6}, then the revised constant ξ^* is 8.96×10^{-6}. If the measured strain is greater than 0.001 and the variation of the temperature is smaller than $10\,^{\circ}\mathrm{C}$, comparatively the term $\xi^*\Delta T$ in Eq. (10.13) is one order of magnitude smaller than that of the strain, and the temperature compensation would be unnecessary in some cases.

10.4 Simultaneous measurements of strain and temperature

10.4.1 Simultaneous measurement of axial strain and temperature

If the internal temperature of the host is unknown and its contribution to the shift of the wavelength is compatible to that of the strain, it is impossible to determine strain and temperature from Eq. (10.9) only. One of the most significant limitations of FBG sensors is their dual sensitivity to temperature and strain. This leads to difficulty in the independent measurements for these two measurands. The main approach is to locate two sensor elements which have different responses to strain and temperature. The sensor schemes are based on the combination of FBGs with different grating types, such as FBGs with different diameter, different Bragg wavelength, different codope, hybrid

Aluminium tube
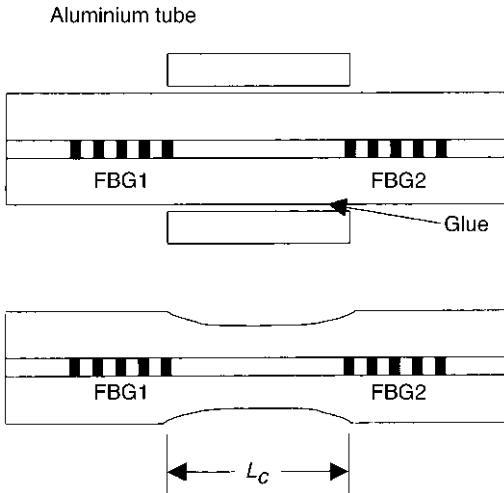
10.4 Structures of FBG cavity sensors: (a) FBG Fabry–Perot cavity, (b) FBG slightly tapered cavity.

FBGs and long period fibre grating, Fabry–Perot cavity, stimulated Brillouin scattering or fibre polarization rocking filter. The observables may be Bragg wavelength, intensity, Brillouin frequency or polarization rocking resonant wavelength.[12–19] This subsection introduces simultaneous axial strain and temperature measurements by using an FBG Fabry–Perot cavity[20,21] or superstructured FBGs.[22]

The structure of a FBG Fabry–Perot cavity sensor is shown in Fig. 10.4(a), which consists of two identical FBGs separated by a short cavity with a length of L_c. If the reflectivity of the two FBGs, $R_g(\lambda)$, is small, the reflection spectrum of the FBG Fabry–Perot cavity sensor, $R_{gc}(\lambda)$, is approximately given by:

$$\left.\begin{array}{l} R_{gc}(\lambda) = a_c R_g(\lambda) F(\lambda) \\ F(\lambda) = 1 + \cos[\phi(\lambda)] = 1 + \cos(4\pi n_c L_c/\lambda) \end{array}\right\} \qquad [10.14]$$

where a_c is a constant, $F(\lambda)$ is an interference of the cavity, $\phi(\lambda)$ is the phase difference between the light reflected by the two FBGs, and n_c is the effective refractive index of the section. The reflection spectrum of the FBG Fabry–Perot cavity sensor is modulated by the cavity phase change. As a result, strain and temperature are encoded into the Bragg wavelength shift and the variation in the cavity's phase difference or optical path. The change in the phase difference can be decoded by measuring the change in the total reflected power or the reflection spectrum profile of light from the sensor.

When a minimum of $F(\lambda)$ occurs within the grating's main reflection band, the FBG Fabry–Perot cavity reflection spectrum is split into two peaks, one

on each side of the Bragg wavelength λ_B. If this minimum $\lambda_{\min}$ coincides with λ_B the intensities of the two peaks become equal. With applied strain or temperature, both the spectrum and the interference function as a result of change in the phase difference variation. The respective shifts of λ_B and $\lambda_{\min}$ can be expressed by:

$$\begin{pmatrix} \Delta\lambda_B/\lambda_B \\ \Delta\lambda_{\min}/\lambda_{\min} \end{pmatrix} = \begin{pmatrix} K_{1T} & K_{1\xi} \\ K_{2T} & K_{2\xi} \end{pmatrix} \begin{pmatrix} \Delta T \\ \varepsilon \end{pmatrix} \qquad [10.15]$$

where K_{iT} and $K_{i\xi}$ are the temperature and strain coefficients of the FBG ($i = 1$) and the cavity ($i = 2$) sections, respectively. If the two sections have equal coefficients such as $K_{1\xi} = K_{2\xi}$ and $K_{1T} = K_{2T}$, the relative position between $\lambda_{\min}$ and λ_B will not change with applied strain or temperature. In this case the reflection spectrum of the FBG Fabry–Perot cavity sensor shifts, but its profile remains unchanged. Thus temperature and strain cannot be determined separately. However, if the FBG and cavity sections have different strain and temperature coefficients, that is $K_{1\xi} > K_{2\xi}$ or $K_{1T} > K_{2T}$, λ_B will move at a faster rate than $\lambda_{\min}$. This results in a reduction in the intensity of peak 1 and an increase in the intensity of peak 2 when strain or temperature increases. When λ_B increases to coincide at the next maximum of $F(\lambda)$ at $\lambda_{\max}$, peak 2 reaches a maximum value and peak 1 vanishes. Further increase in strain or temperature will result in two peaks in the FBG Fabry–Perot cavity reflection spectrum, but in this case the intensity of peak 2 (corresponding to the longer wavelength) will decrease, whereas the intensity of peak 1 (corresponding to the shorter wavelength) increases. Therefore, the intensity of the two peaks changes periodically with strain and temperature.

The intensity fluctuation of the light source can be eliminated by introducing a normalized parameter $M = (I_{P1} - I_{P2})/(I_{P1} + I_{P2})$, where I_{P1} and I_{P2} are the respective intensities of peaks 1 and 2. If the relationship between $\Delta\lambda_P$, M, ε and ΔT is assumed to be linear, then the two measurands can be determined simultaneously by measuring the changes in M and the wavelength shift $\Delta\lambda_P$ of either peak 1 or peak 2 with respect to strain and temperature:

$$\begin{pmatrix} \Delta\lambda_P \\ \Delta M \end{pmatrix} = \begin{pmatrix} A_{1T} & A_{1\xi} \\ A_{2T} & A_{2\xi} \end{pmatrix} \begin{pmatrix} \Delta T \\ \varepsilon \end{pmatrix} \qquad [10.16]$$

In order that the strain and temperature coefficients of the cavity section are different from those of the grating sections, a short (1 mm long) and thin aluminium tube (with an inside diameter of 0.3 mm and wall thickness of 0.15 mm) was glued onto the cavity section. This section is more difficult to stretch than the grating sections, and thus its strain coefficient is correspondingly smaller, so that $K_{2\xi} < K_{1\xi}$. On the other hand, its temperature coefficient becomes larger ($K_{2T} > K_{1T}$). This is because the thermal expansion coefficient

of aluminium (23.5×10^{-6}/°C) is much larger than that of the silica glass fibre (0.55×10^{-6}/°C), and expansion of the aluminium tube due to temperature rise induces additional strain to the cavity section.

Figure 10.4(b) shows another FBG Fabry–Perot cavity structure, that is an FBG tapered cavity sensor, in which the cavity section is tapered slightly. The maximum change of diameter at the cavity section is smaller than 15%, hence no obvious changes in transmission and mode-effective refractive index are induced. The tapered cavity section possesses the same strain and temperature coefficients as those of the grating section. However, the average strain suffered by the tapered cavity (ξ_c) becomes larger than that at the grating section (ξ), which is given by $\xi_c = \eta\xi$, where η is an average ratio of cross-sectional areas between the grating and cavity sections. The relative movement between $F(\lambda)$ and $R_g(\lambda)$ remains zero when the temperature changes, therefore the spectral profile is only sensitive to the strain applied along the sensor:

$$\begin{pmatrix} \Delta\lambda_B/\lambda_B \\ \Delta\lambda_{min}/\lambda_{min} \end{pmatrix} = \begin{pmatrix} \alpha_1 & \beta_1 \\ \alpha_1 & \eta\beta_1 \end{pmatrix}\begin{pmatrix} \Delta T \\ \varepsilon \end{pmatrix} \qquad [10.17]$$

where α_1 and β_1 are the temperature and strain coefficients of the grating section, respectively.

Superstructured FBG sensors were developed for this purpose,[22] which have advantages of easier manufacturing and no need to alter the mechanical properties and geometry of fibre sensor. FBG sensors generally consist of a single FBG or a combination of FBGs written in low-birefringent optical fibre. In the former case, the Bragg wavelength shift can be used to measure the axial component of strain or a change in temperature. In the latter case, axial strain and temperature can be simultaneously determined according to the Bragg wavelength shifts, or the Bragg wavelength shifts and the intensities.

10.4.2 Simultaneous measurement of multi-axial strain and temperature

10.4.2.1 Polarization-maintaining (PM) FBG

The transverse strain-induced wavelength sensitivity of FBGs in silica optical fibres is low. For instance, in lateral compression, the changes in fibre birefringence are smaller than 10^{-6}. This level of birefringence corresponds to wavelength separations much smaller than the typical bandwidth of an FBG. However, we have shown in Section 10.3.1 that the sensitivity factor is a function of the two principal transverse strains and axial strain, which are normally unknown. The needs are apparent for multi-axial measurements of strain and temperature.

FBGs were written in a polarization-maintaining fibre for the measurement of lateral strains.[23–26] A polarization-maintaining fibre may consist of a circular core and inner cladding surrounded by an elliptical stress-applying region. Birefringence is induced by thermal stresses generated during the cool-down from the drawing temperature due to the geometric asymmetry of the stress-applying region. This stress-induced birefringence leads to different propagation constants for the two orthogonal polarization modes in the fibre. The x and y axes are parallel to the fast and slow axes of the principal polarization axes of the fibre, respectively, which correspond to the minor and major axes of the elliptical stress-applying region. Polarization-maintaining fibre has an initial birefringence that is sufficient to split the grating completely into two separate spectra. Because of the difference in effective refractive indices of the two orthogonal polarization modes, two effective FBGs result in one along the polarization axes by writing one FBG. For the case of low-birefringent FBG, if the temperature sensitivity of the FBG remains constant, the relative Bragg wavelength shifts can be written as:

$$\left.\begin{aligned}
\Delta\lambda_{ax}/\lambda_{ax0} &= \varepsilon_3 - 0.5 \times n_{\text{eff}x}^2[p_{11}\varepsilon_1 + p_{12}(\varepsilon_2 + \varepsilon_3)] \\
\Delta\lambda_{ay}/\lambda_{ay0} &= \varepsilon_3 - 0.5 \times n_{\text{eff}y}^2[p_{11}\varepsilon_2 + p_{12}(\varepsilon_1 + \varepsilon_3)]
\end{aligned}\right\} \qquad [10.18]$$

where λ_{ax} and λ_{ay} are the Bragg wavelength for the two orthogonal polarization modes, respectively, λ_{ax0} and λ_{ay0} are the initial unstrained Bragg wavelength for the two orthogonal polarization modes, respectively, and $n_{\text{eff}x}$ and $n_{\text{eff}y}$ are the effective refractive indices of the two orthogonal polarization modes, respectively. Supposing that the axial strain is known, the relative Bragg wavelength shifts can be written in matrix:

$$\begin{pmatrix} \Delta\lambda_{ax}/\lambda_{ax0} \\ \Delta\lambda_{ay}/\lambda_{ay0} \end{pmatrix} = \begin{pmatrix} K_{11} & K_{12} \\ K_{21} & K_{22} \end{pmatrix} \begin{pmatrix} \varepsilon_1 \\ \varepsilon_2 \end{pmatrix} \qquad [10.19]$$

where the coefficient matrix contains p_{11}, p_{12}, ε_3, $n_{\text{eff}x}$ and $n_{\text{eff}y}$. For the case of high-birefringent FBG, such as polarization-maintaining FBG (PM-FBG), the sensor must be calibrated to the finite-element predictions by performing a least-squares fit to determine the coefficient matrix from the measured wavelength data. According to Eq. (10.19), the lateral components of the strain can be determined. In many structures, one would like an FBG sensor that could measure both lateral axes of strain, axial strain and temperature. An approach to solving this problem is to use dual overlaid FBGs at different Bragg wavelengths written onto a PM fibre.[27] If two FBGs of different Bragg wavelengths, such as 1300 nm and 1550 nm, were written at a single location in a PM fibre, four effective FBGs result in one along the corresponding polarization axis and at corresponding Bragg wavelength. The relative Bragg wavelength shifts can be written as:

$$\begin{pmatrix} \Delta\lambda_{ax}/\lambda_{ax0} \\ \Delta\lambda_{ay}/\lambda_{ay0} \\ \Delta\lambda_{bx}/\lambda_{bx0} \\ \Delta\lambda_{by}/\lambda_{by0} \end{pmatrix} = \begin{pmatrix} K_{11} & K_{12} & K_{13} & K_{14} \\ K_{21} & K_{22} & K_{23} & K_{24} \\ K_{31} & K_{32} & K_{33} & K_{34} \\ K_{41} & K_{42} & K_{43} & K_{44} \end{pmatrix} \begin{pmatrix} \varepsilon_1 \\ \varepsilon_2 \\ \varepsilon_3 \\ \Delta T \end{pmatrix} \qquad [10.20]$$

where λ_{bx} and λ_{by} are the Bragg wavelength for the two orthogonal polarization modes of the second FBG, respectively, and λ_{bx0} and λ_{by0} are the initial unstrained Bragg wavelength for the two orthogonal polarization modes of the second FBG, respectively. Assuming linearity in sensor response and that the element of the 4×4 coefficient matrix is independent of strain and temperature, and the matrix is not singular, the elements of the matrix can be determined by performing separate experimental and least-squares fitting calibrations of the response of the sensor to lateral strain, to axial strain and to temperature changes.

10.4.2.2 π-Phase-shifted FBG

Another approach is to use π-phase-shifted FBGs.[28,29] If a regular FBG is irradiated with UV light at a certain region in the middle of the FBG, the refractive index in the region is raised. Such processing produces two FBGs out of phase with each other, which act as a wavelength-selective Fabry–Perot resonator, allowing light at the resonance to penetrate the stop-band of the original FBG. The resonance wavelength depends on the size of the phase change. When the shifted phase is equal to π at a wavelength λ_0 in the stop-band of the original FBG, the strong reflections from the two FBG sections are out of phase, resulting in strong transmission at this wavelength. This post-processing FBG is called π-phase-shifted FBG (π-FBG). The transmission window of π-FBG can be made very narrow and is split in two when the FBG is birefringent. This sharpness permits very high accuracy measurement of the FBG birefringence. Furthermore, the birefringence required for separating the peak is much smaller than for regular FBGs and can be provided by the intrinsic birefringence of an FBG written in non-PM fibre.

The fibre has birefringence in the absence of an external load, of which several factors, such as geometric, UV-induced and stress-induced, may be at the origin. However, for mathematical convenience, it is assumed that the initial birefringence in the FBG is due to a residual strain state in the fibre core that is described by the principal strains ε_{10} and ε_{20} $(\varepsilon_{10} > \varepsilon_{20})$. These principal strains are in directions perpendicular to each other and to the fibre axis, and direction 1 makes an angle ϕ with the x axis. According to Eq. (10.18), the wavelength separation can be expressed as:

$$\Delta\lambda_0 = \Delta\lambda_{10} - \Delta\lambda_{20} \approx 0.5\lambda_0[(n_{\text{eff}\,1} + n_{\text{eff}\,2})/2]^2$$
$$(p_{12} - p_{11})(\varepsilon_{10} - \varepsilon_{20}) \qquad [10.21]$$

The new wavelength separation can be obtained by a function of ϕ[28,29]

$$\Delta\lambda(\phi) = a + b\cos(2\phi) \qquad [10.22]$$

where a and b are positive values which are independent of ϕ. Thus, the larger the angle ϕ is, the lower the sensitivity to lateral strain.

10.5   Measurement effectiveness

For the FBGS to be an ideal embedded strain sensor in a textile composite, the following conditions will have to be met:[30] (1) the integrated optic fibre has little effect on the host strain field; (2) the axial strain of optic fibre ε_1 can represent the nearby host strain in the optic fibre direction; and (3) the effective Poisson's ratio υ^* is constant during the measurement period. The embedded-optic-fibre–host system can be illustrated[31] as a composite comprising a cylindrical fibre and two concentric shell layers, with fibre, coating and host from the centre to the outer surface (Fig. 10.5). The height of the composite cylinder is $2H$, the radius of the fibre is R_1, which is also the interior radius of coating, R_2 is the outer radius of the coating and the inner radius of the host, and R_3 is the outer radius of the host. The following basic assumptions have been made so that the case can be simplified as an axial-symmetric problem: (1) The optical fibre, fibre coating and host are linear elastic. (2) The thermal expansion coefficients of fibre, coating and host are constants. (3) There is no discontinuity in displacement at the interfaces of fibre and coating, coating and host under loading. (4) Thermal load is uniform in the whole composite cylinder. (5) The two ends $(z = \pm H)$ are assumed to be free from any external force and there is no constraint on displacement.

10.5.1 General views of the normalized strain distribution

Figure 10.6(a), (b) and (c) illustrate the normalized strain distribution in the fibre, host and coating, respectively, along the fibre axial direction with various values of radius r. Figure 10.6(a) shows that the normalized strain of
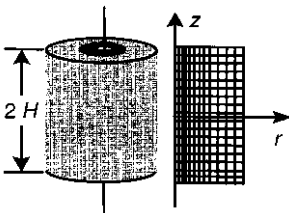
10.5 Three-layer composite model of host, coating, and fibre.
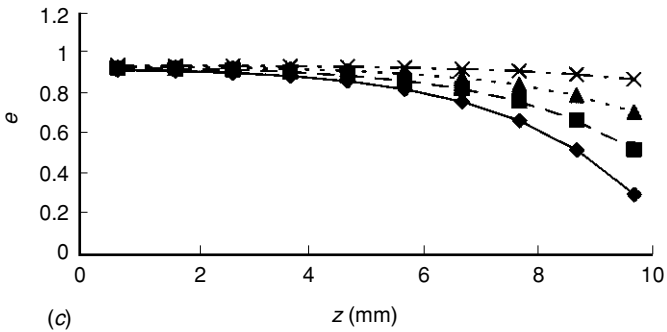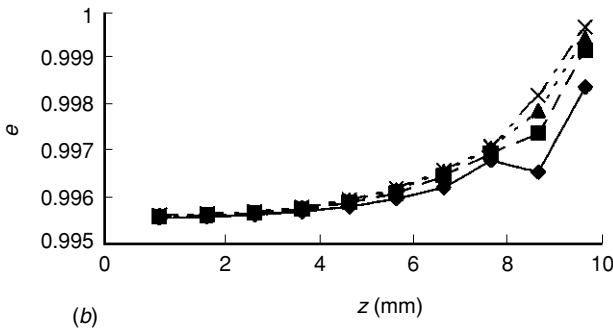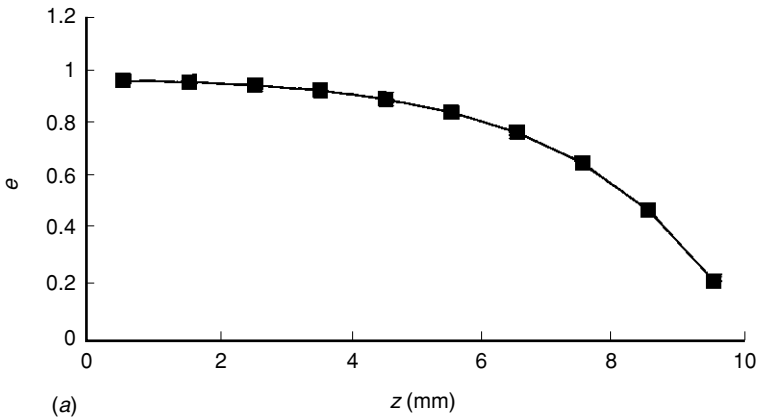
10.6 Strain distribution in the embedded optic fibre–host sytem:
(a) distribution of fibre's axial strain at various radial positions, —◆—
0.007875; —■— 0.023625; —▲— 0.039375; —×— 0.055125;
(b) distribution of host's axial strain at various radial positions, —◆—
0.248; —■— 0.498; —▲— 0.748; —×— 0.998; (c) distribution of coating's
axial strain at various radial positions, —◆— 0.0705; —■— 0.0855; —▲—
0.1005; —×— 0.1155.

fibre declines with increasing length z. Because the thermal expansion coefficient of the optic fibre is more than one order of magnitude smaller than that of the host, the strain level of the optic fibre depends largely on the restriction of the host. As the middle part of the optic fibre is restricted more than the parts near the two ends, the strain of the middle optic fibre is closer to that of the host without the embedded fibre sensor ($e = 1$). The strain distribution curves are identical, regardless of the radial position in the fibre, thus the strain of the fibre can be regarded as a function of z only.

Figure 10.6(b) shows the reverse trends of strain distribution in the host. The strain level of the middle host is lower than that of the host near the boundary, which is because the middle host is restricted more by the fibre and the host near the boundary can expand more freely under a thermal load. The normalized strain values of the host are very close to 1 ($0.995 < e < 1$), which implies that the host with the embedded fibre sensor has a strain field very close to that without the embedded optic fibre.

Because of its lower elastic modulus, the strain distribution of the coating is significantly affected by both the fibre and the host, as shown in Fig.10.6(c). The strain distribution along z is similar with that of the fibre when r approaches R_1, and the strain near the outer surface of the coating varies little along z, like that of the host.

10.5.2 Effects of parameters on effectiveness coefficient

The term H_{95} has been introduced,[31] at which e has a value of 0.95. The physical meaning of H_{95} is that only when the z of the optic fibre grating is smaller than H_{95} is the measurement result of the fibre effective. The length of the zone represents the limits of effective measurement of host strain by an embedded FBGS. The longer the zone length, the more effective an FBGS in a host. Thus the relative length of the effective zone is defined as the effectiveness coefficient β by:

$$\beta = \frac{H_{95}}{H}$$

The effectiveness coefficient is influenced by a number of factors, the elastic modulus, Poisson's ratio of coating, tension stiffness ratio, the thickness of composite etc.[30,31] Figure 10.7 shows that increasing E_c leads to a sharp increment in β when E_c varies from 0.045 to 1 GPa. The curve then reaches a plateau and the effect on β becomes very small. Thus $E_c = 1$ GPa can be regarded as a threshold value for the specified conditions.

Figure 10.8 plots the effective Poisson's ratio of the optic fibre against the fibre length. Within a range from zero to 7 mm, the effective Poisson's ratio
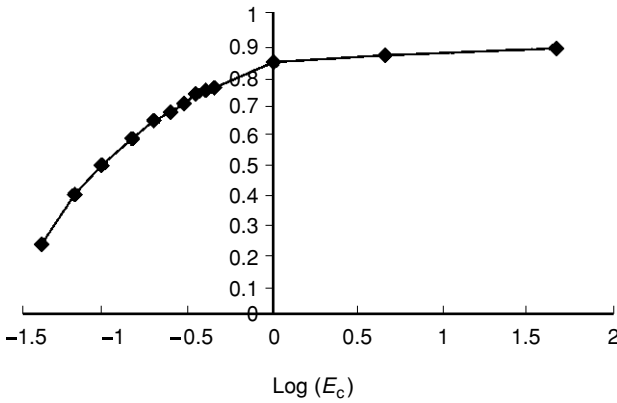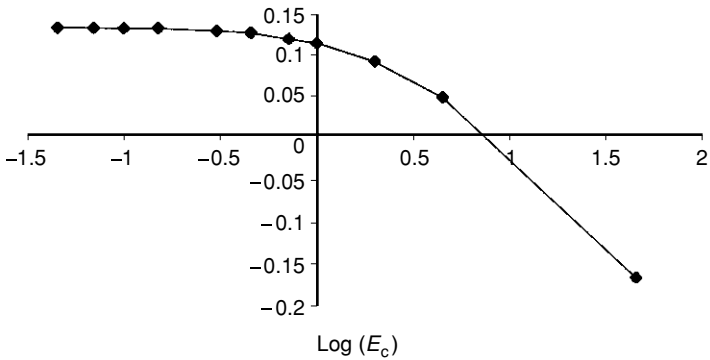
10.7 Effect of elastic modulus of coating on the effectiveness coefficient β of optic fibre.
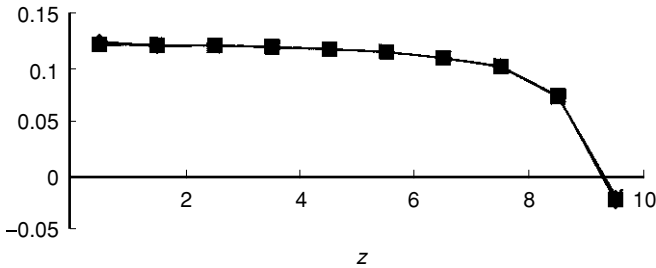
10.8 Distribution of fibre's effective Poisson's ratio along the fibre length at various radial positions.

declines slightly with the increment of z. Thus it can be regarded as a constant along the z axis except for the short portion near the boundary. The value of v^* near $z = 0$ is 0.13 which is not equal to the Poisson's ratio of the fibre (0.17). This indicates that the transverse strain of the optic fibre is not dominated by the host strain (otherwise it should be close to -1) but by the Poisson's ratio of the fibre.

In the particular case under our investigation, the elastic modulus of the coating should be equal to or greater than the threshold value $f = 0.78\,\text{GPa}$, if the measurement effectiveness is concerned (see Fig. 10.7). However, the increment of E_c will affect the value of the effective Poisson's ratio, v^*, then the sensitivity factor, f. Figure 10.9 plots v^* as a function of E_c, which exhibits the reversed trend compared with that of the effectiveness β. When the coating modulus is smaller than, or equal to, the threshold value of $1\,\text{GPa}$, the variation of v^* is rather small. By considering the effects of the coating elastic modulus on both measurement effectiveness and the effective Poisson's ratio,

10.9 Effect of elastic modulus of coating on fibre's effective Poisson's ratio.

the optimal coating modulus should be chosen as the threshold value $E_c = 1\,\text{GPa}$. This case illustrates the necessity of selecting optimal material properties of coating in order to make effective measurements.

10.6   Reliability of FBGs

A single-mode silica optic fibre has a typical cladding diameter of 125 microns and an outer diameter of 250 microns. It can be introduced into a textile preform in its manufacturing processes such as weaving, knitting and braiding. Alternatively, it can be introduced at the consolidation process of the textile composites. In both cases, caution should be exercised when integrating it into the textile structure. Apart from avoiding the damage to the optic fibre during manufacturing processes, the reliability of an embedded fibre Bragg grating sensor is influenced by a number of other factors as follows:[32]

1   Grating-making method: an optic fibre is normally decoated around the grating location before UV pulse laser exposure and recoated afterward. During the decoating and UV irradiation processes, the optic fibre may get damaged, as shown in Chapter 8. Further, the new coat may cause some variation in the fibre. The sensitivity to strain may be different for FBG sensors, even with the same central reflecting wavelength.
2   Location and direction of sensors in composite hosts: usually the FBG sensor is used to measure certain positional and directional normal strain in the host. However, in the procedure of embedding the FBG sensor into the composite host, some deviation of the optic fibre sensor may occur from the designed position and direction. To reduce the measurement error, determination of the real location of the grating of FBG sensors inside the composite may be a key issue, especially when the sensors are

embedded in a large gradient strain field such as near the tip of a crack. Furthermore, it is very difficult to precisely detect the real position and direction of the fibre grating sensor after it is embedded into a composite. The levels of errors induced by the deviation of position and direction of the sensors will be given in Section 10.7.

3   The interfaces of fibre/coating and coating/resin: stress concentration exists around the interfaces and may cause cracks, which may affect the measurement results. Researchers have introduced a debonding phenomenon into the interfaces between fibre and coating as well as between coating and host when fabricating the fibre Bragg optic strain sensors and integrating them into a laminated composite beam.[33] The study showed that the dual-ended sensors are reliable in cyclic bending deformation, while the single-ended sensors are not when their interface bonding fails. To reduce the measurement error, determination of the real location of the grating of FBG sensors inside the composite may be a key issue for future work, especially when the sensors are embedded in a large gradient strain field such as near the tip of a crack.

4   The environment and working conditions to which a textile composite is subject, and how long it is subject to them, will greatly influence the selection and integration of fibre optic sensors. The analysis of measurement effectiveness in the previous section is based on the composite model assuming perfect interfaces between the coating and fibre as well as between the coating and host. Another condition is that the strain measured by the optic fibre sensor is at a predetermined position and in a predetermined direction. Hence, the following section will investigate their effects when these assumed conditions are not met.

10.7   Error of strain measurement due to deviation of position and direction

10.7.1 Deviation of direction

Assume the principal strains in a structure are ε_1, ε_2 and ε_3. If an FBG sensor is embedded in the structure and the angles between the sensor and principal strains are α_1, α_2 and α_3, the strain induced along the FBG sensor is:

$$\varepsilon = [\cos\alpha_1 \quad \cos\alpha_2 \quad \cos\alpha_3] \begin{bmatrix} \varepsilon_1 & 0 & 0 \\ 0 & \varepsilon_2 & 0 \\ 0 & 0 & \varepsilon_3 \end{bmatrix} \begin{bmatrix} \cos\alpha_1 \\ \cos\alpha_2 \\ \cos\alpha_3 \end{bmatrix} \qquad [10.23]$$

$$= \varepsilon_1 \cos^2\alpha_1 + \varepsilon_2 \cos^2\alpha_2 + \varepsilon_3 \cos^2\alpha_3$$

where $\cos^2\alpha_1 + \cos^2\alpha_2 + \cos^2\alpha_3 = 1$. The strain measured in the sensor is a

function of the principal strains and the angles between them and the sensor. In practice, when a sensor is embedded in the structure, it is most likely to show deviation between the sensor and desired direction. Suppose the deviations of the sensor are $\Delta\alpha_1$, $\Delta\alpha_2$ and $\Delta\alpha_3$, then the strain in the sensor will be:

$$\varepsilon_{\Delta\alpha} = \varepsilon_1 \cos^2(\alpha_1 + \Delta\alpha_1) + \varepsilon_2 \cos^2(\alpha_2 + \Delta\alpha_2) + \varepsilon_3 \cos^2(\alpha_3 + \Delta\alpha_3)$$
[10.24]

According to Eq. (10.24), if one wants to measure one of the principal strains, the simplest method is to place sensors along the direction of the desired strain. For example, if ε_1 is desired, the sensor will be placed along this direction. Then we have $\alpha_1 = 0$ and $\alpha_2 = \alpha_3 = \pi/2$. The influence of other strains (ε_2 and ε_3) will be cancelled. If the deviations between the sensor and the desired direction are $\Delta\alpha_1$, $\Delta\alpha_2$ and $\Delta\alpha_3$, the strain along the sensor will be:

$$\begin{aligned} \varepsilon'_{\Delta\alpha} &= \varepsilon_1 \cos^2 \Delta\alpha_1 + \varepsilon_2 \cos^2(\pi/2 + \Delta\alpha_2) + \varepsilon_3 \cos^2(\pi/2 + \Delta\alpha_3) \\ &= \varepsilon_1 \cos^2 \Delta\alpha_1 + \varepsilon_2 \sin^2 \Delta\alpha_2 + \varepsilon_3 \sin^2 \Delta\alpha_3 \end{aligned}$$
[10.25]

The relative error between the measured and real values of strain is:

$$error_1 = \left| \frac{\varepsilon'_{\Delta\alpha} - \varepsilon_1}{\varepsilon_1} \right| = \left| \frac{\varepsilon_1 \cos^2 \Delta\alpha_1 + \varepsilon_2 \sin^2 \Delta\alpha_2 + \varepsilon_3 \sin^2 \Delta\alpha_3 - \varepsilon_1}{\varepsilon_1} \right|$$
[10.26]

If $\Delta\alpha_1$, $\Delta\alpha_2$ and $\Delta\alpha_3$ are small quantities, Eq. (10.26) can be expressed as:

$$error_1 = \left| \frac{- \varepsilon_1 \Delta\alpha_1^2 + \varepsilon_2 \Delta\alpha_2^2 + \varepsilon_3 \Delta\alpha_3^2}{\varepsilon_1} \right| \leq |\Delta\alpha_1^2| + \left| \frac{\varepsilon_2}{\varepsilon_1} \Delta\alpha_2^2 \right| + \left| \frac{\varepsilon_3}{\varepsilon_1} \Delta\alpha_3^2 \right|$$
[10.27]

In Eq. (10.27), the third and higher orders of deviations are omitted. The measurement error is quadratic to the deviations in the orientation angles.

10.7.2 Deviation of position

The strain field of a structure is related to the position and the deformation of the structure. Suppose the strain at point (x, y, z) can be expressed as $\varepsilon = \mathbf{f}(x, y, z, \delta)$, where ε is a tensor and δ represents the displacement vector of the structure. The variation of strain due to the deviations of the position $(\Delta x, \Delta y, \Delta z)$ can be expressed as:

$$\begin{aligned} \Delta\varepsilon = {}& \frac{\partial \mathbf{f}(x, y, z, \delta)}{\partial x} \cdot \Delta x + \frac{\partial \mathbf{f}(x, y, z, \delta)}{\partial y} \cdot \Delta y \\ &+ \frac{\partial \mathbf{f}(x, y, z, \delta)}{\partial z} \cdot \Delta z + E(\Delta x, \Delta y, \Delta z) \end{aligned}$$
[10.28]

where $E(\Delta x, \Delta y, \Delta z)$ is the second and higher-order quantities of the position deviation $(\Delta x, \Delta y, \Delta z)$. When the deviations are small and $E(\Delta x, \Delta y, \Delta z)$ can be omitted, Eq. (10.28) can be simplified as:

$$\Delta \varepsilon \approx \frac{\partial \mathbf{f}(x, y, z, \delta)}{\partial x} \cdot \Delta x + \frac{\partial \mathbf{f}(x, y, z, \delta)}{\partial y} \cdot \Delta \ y + \frac{\partial \mathbf{f}(x, y, z, \delta)}{\partial z} \cdot \Delta z \qquad [10.29]$$

For a cantilever beam, if a concentrated load acts at its free end, the axial strain of an arbitrary point (x, y, z) in the beam due to the normal displacement δ of the free end is:

$$\varepsilon_1(x, y, z) = \frac{3\delta}{L^3}(L - x)z \qquad [10.30]$$

where L is the length of the beam, x is the location of the point along the beam, y is the location of the point along the y-direction, and z is the distance between the point and the neutral axis of the beam.

The strain in the beam is independent of the position of y. That means the deviation of y will not influence the strain measurement. If there are any deviations of the test point $(\Delta x, \Delta y, \Delta z)$, according to Eq. (10.29) the variation of the strain will be:

$$\Delta \varepsilon_1 = -\frac{3\delta z}{L^3} \cdot \Delta x + \frac{3\delta(L - x)}{L^3} \cdot \Delta z \qquad [10.31]$$

The relative error of strain deduced from the position deviations is:

$$error_2 = \left| \frac{\Delta \varepsilon}{\varepsilon(x, y, z)} \right| \leq \left| \frac{\Delta x}{L - x} \right| + \left| \frac{\Delta z}{z} \right| \qquad [10.32]$$

If the sensors are placed near the fixed end $(x = x_{min} \approx 0)$ and far from the neutral axis $(z = z_{max} \approx h/2, h$ is the height of the cantilever beam) of the beam, the measurement error will be the minimum.

10.7.3 Deviation of both direction and position

If deviations of direction and position occur simultaneously, then the total relative error is:

$$error_{total} = error_1 + error_2 \leq |\Delta \alpha_1^2| + \left| \frac{\varepsilon_2}{\varepsilon_1} \Delta \alpha_2^2 \right| + \left| \frac{\varepsilon_3}{\varepsilon_1} \Delta \alpha_3^2 \right|$$
$$+ \left| \frac{\Delta x}{L - x} \right| + \left| \frac{\Delta z}{z} \right| \qquad [10.33]$$

From Eq. (10.33) we know that, in order to obtain an accurate measurement result, the deviations of direction and position should be as small as possible.

This derivation is more suitable for the surface-mounted FBGs. If

embedded in a composite, the localized heterogeneity will normally lead to a complicated strain field. If the strain is not uniformly distributed along FBG, grating apodization occurs. The strain may induce birefringence which may cause peak split. Hence, the analysis of measurement error must consider at least the above-mentioned factors.
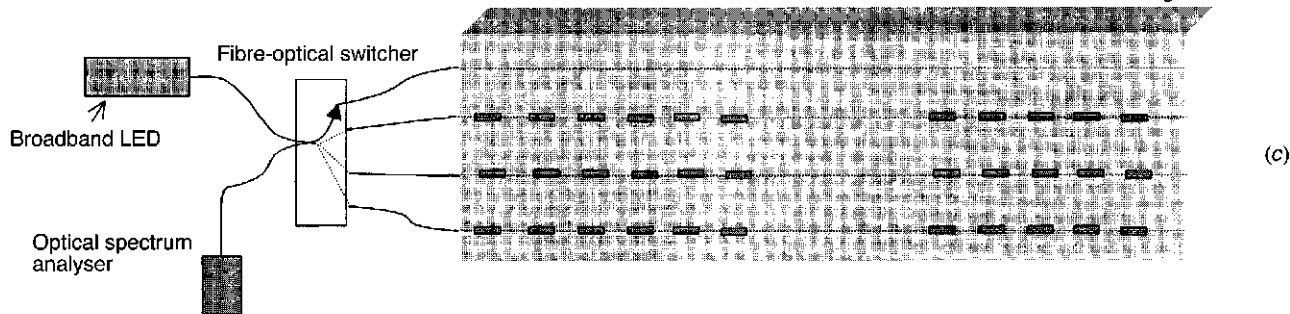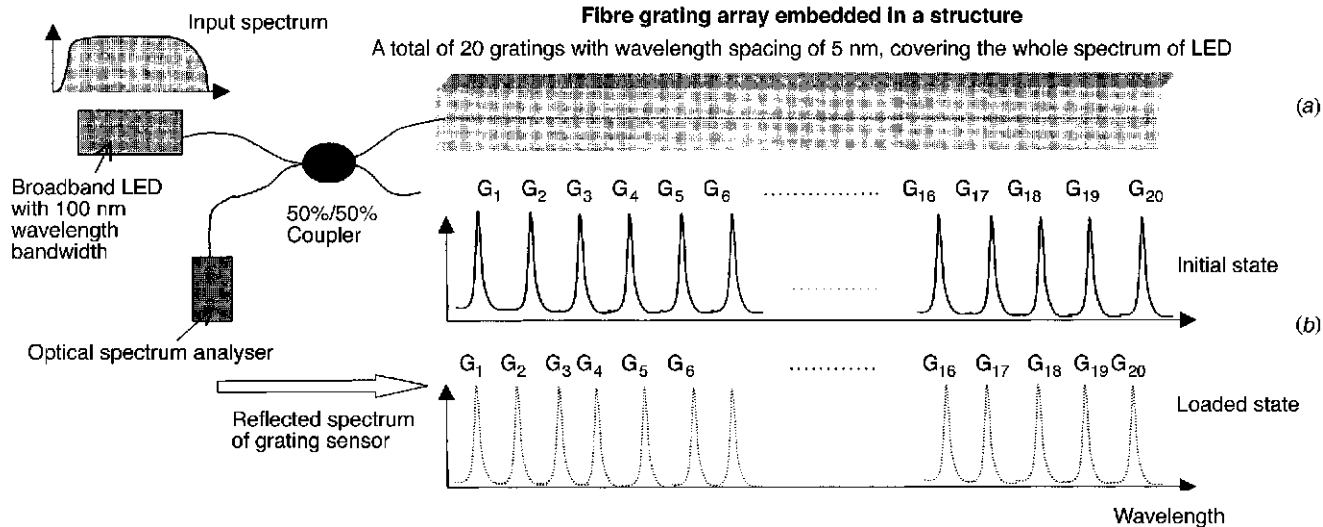
10.8   Distributed measurement systems

By the means of measuring the shift of the peak wavelength of the reflective spectrum, the average strain over the whole grating length is determined, rather than the distribution of the strain. In many applications, the distribution of strain and temperature is the major concern, thus a number of methods can be implemented to serve this purpose. The grating length of FBGs can be made very short (e.g. 2 mm), thus the strain measured by the shift wavelength of the reflective spectrum can be regarded as a localized strain. The FGB arrays render themselves as ideal candidates for multi-point or quasi-distributive measurements by the multiplexing techniques used for several other optical fibre sensors, such as wavelength-division-multiplexing (WDM),[34] time-division-multiplexing (TDM) and spatial-division-multiplexing (SDM). Detailed reviews have been given by Rao,[35] Kersey et al.[36] and Othonos and Kalli.[37] Figure 10.10 shows a schematic diagram of the measurement systems, consisting of a broad-band LED, a coupler or optic switch, an optical analyser, and an embedded multiplexing FBG array by which we carried out our pseudo-distributed measurement of strain-temperature in textile composites.

In simple cases, if it is monotonic, the strain distribution can be determined along the grating by analysing the reflection spectrum. Volanthen and his colleagues developed a measurement system of distributed grating sensors to measure the wavelength and reflectivity of gratings as functions of time delay.[38–40] By using low-coherence reflectometry, this technique was applied to three-point bending experiments of a textile composite beam embedded with FBGs.[30]

10.9   Conclusions

In conclusion, fibre optic sensors are ideal candidates to be embedded in textile structural composites for monitoring manufacturing processes and internal health conditions. The sensors provide an effective means by which the distributions of a number of physical parameters, such as temperature, stress/strain, thermal expansion, pressure, etc., can be quantitatively determined. In integrating the sensors into textile composites, apart from the properties of the sensors themselves, the reliability of the sensors and sensing scheme as well

Input spectrum

Fibre grating array embedded in a structure
A total of 20 gratings with wavelength spacing of 5 nm, covering the whole spectrum of LED

Broadband LED
with 100 nm
wavelength
bandwidth

50%/50%
Coupler

Optical spectrum analyser

G_1 G_2 G_3 G_4 G_5 G_6 .... G_{16} G_{17} G_{18} G_{19} G_{20}

Initial state

Reflected spectrum
of grating sensor

G_1 G_2 G_3 G_4 G_5 G_6 .... G_{16} G_{17} G_{18} G_{19} G_{20}

Loaded state

Wavelength

Fibre-optical switcher

Broadband LED

Optical spectrum
analyser

(a)

(b)

(c)

10.10 Wavelength-division-multiplexing systems by FBG arrays embedded in composites.

as the interaction between sensors and composites are very important issues to consider.

Acknowledgements

References

1 Du C W, Tao X M, Tam Y L and Choy C L, 'Fundamentals and applications of optical fiber Bragg grating sensors to textile composites', *J. Composite Struct.*, 1998, **42**(3), 217–30.
2 Matthews L K (ed.), *Smart Structures and Materials 1995*, *Smart Systems for Bridges*, *Structures*, *and Highways*, *SPIE*, 1995, **2446**.
3 Merzacher C I, Kersey A D and Friebele E J, 'Fibre optic sensors in concrete structures: a review', *Smart Mater. Struct.*, 1996, **5**, 196–208.
4 Hayes S A, Brooks D, Liu T Y, Vicker S and Fernando G F, 'In-situ self-sensing fibre reinforced composites', *Smart Structures and Materials 1996*, *SPIE*, **2718**, 376–84.
5 Hong C S, Kim C G, Kwon I and Park J W, 'Simultaneous strain and failure sensing of composite beam using an embedded fibre optic extrinsic Fabry–Perot sensor', *Smart Structures and Materials 1996*, *SPIE*, 1996, **2718**, 122–33.
6 Badcock R A and Fernando G F, 'Intensity-based optical fibre sensor for fatigue damage detection in advanced fibre-reinforced composites', *Smart Mater. Struct.*, 1995, **4**(4), 223–30.
7 Udd E, Fiber optic sensor overview. In *Fiber Optic Smart Structures*, ed. E Udd, John Wiley, 1995.
8 Measures R M, Fiber optic strain sensing. In *Fiber Optic Smart Structures*, ed. E Udd, John Wiley, 1995.
9 Butter C D and Hocker G P, 'Fiber optics strain gauge', *Appl. Opt.*, 1992, **1370**, 189–96.
10 Sirkis J S and Haslach H W Jr, 'Full phase-strain relation for structurally embedded interferometric optic fiber sensors', *Proc. SPIE*, 1990, **1370**, 248–59.
11 Jackson D A and Jones J D C, 'Fibre optic sensors', *Pot. Acta*, 1986, **33**, 1469–503.
12 Takahashi S and Shibata S, 'Thermal variation of attenuation for optical fibers', *J. Non-crystal. Solids*, 1979, **30**, 359–70.
13 Akhavan Leilabady P, Jones J D C and Jackson D A, *Optics Lett.*, 1985, **10**, 576.
14 Friebele E J, Putnam M A, Patrick H J et al., 'Ultrahigh-sensitivity fiber-optic strain and temperature sensor', *Optics Lett.*, 1998, **23**, 222–4.
15 Chan C C, Jin W, Rad A B et al., 'Simultaneous measurement of temperature and strain: an artificial neural network approach', *IEEE Photon. Technol. Lett.*, 1998, **10**, 854–6.

16 James S W, Dockney M L and Tatam R P, 'Simultaneous independent temperature and strain measurement using in-fiber Bragg grating sensors', *Electron. Lett.*, 1996, **32**, 1133–4.

17 Xu M G, Archambault J L, Reekie L et al., 'Discrimination between strain and temperature effects using dual-wavelength fiber grating sensors', *Electron. Lett.*, 1994, **30**, 1085–7.

18 Cavaleiro P M, Araújo F M, Ferreira L A et al., 'Simultaneous measurement of strain and temperature using Bragg gratings written in germanosilicate and boron-codoped germanosilicate fibers', *IEEE Photon. Technol. Lett.*, 1999, **11**, 1635–7.

19 Patrick H J, Williams G M, Kersey A D et al., 'Hybrid fiber Bragg grating/long period fiber grating sensor for strain/temperature discrimination', *IEEE Photon. Technol. Lett.*, 1996, **8**, 1223–5.

20 Du W C, Tao X M and Tam H Y, 'Fiber Bragg grating cavity sensor for simultaneous measurement of temperature and strain', *IEEE Photon. Technol. Lett.*, 1999, **11**, 105–7.

21 Du W C, Tao X M and Tam H W, 'Temperature independent strain measurement with a fiber grating tapered cavity sensor', *IEEE Photon. Technol. Lett.*, 1999, **11**(5), 596–8.

22 Guan B O, Tam H Y, Tao X M and Dong X Y, 'Simultaneous strain and temperature measurement using a superstructure fiber Bragg grating', *IEEE Photon. Technol. Lett.*, 2000, **12**(6), 1–3.

23 Kawase L R, Valente L C G, Margulis W et al., 'Force measurement using induced birefringence on Bragg grating', in *Proc. 1997 SBMO/MTT-S International Microwave and Optoelectronics Conference*, **1**, 394–6.

24 Lawrence C M, Nelson D V, Makino A et al., 'Modeling of the multi-parameter Bragg grating sensor', in *Proc. SPIE – Third Pacific Northwest Fiber Optic Sensor Workshop*, **3180**, 42–9.

25 Udd E, Nelson D and Lawrence C, 'Multiple axis strain sensing using fiber gratings written onto birefringent single mode optical fiber', in *Proc. 12th International Conference on Optical Fiber Sensors*, Williamsburg, USA, 1997, 48–51.

26 Udd E, Lawrence C M and Nelson D V, 'Development of a three axis strain and temperature fiber optical grating sensor', in *Proc. SPIE – Smart Structures and Materials 1997: Smart Sensing, Processing, and Instrumentation*, **3042**, 229–36.

27 Udd E, Schulz W L, Seim J M et al., 'Transverse fiber grating strain sensors based on dual overlaid fiber gratings on polarization preserving fibers', in *Proc. SPIE – Smart Structures and Materials 1998: Sensory Phenomena and Measurement Instrumentation for Smart Structures and Materials*, **3330**, 253–63.

28 LeBlanc M, Vohra S T, Tsai T E et al., 'Transverse load sensing by use of pi-phase-shifted fiber Bragg gratings', *Optics Lett.*, 1999, **24**, 1091–3.

29 Canning J and Sceats M G, 'π-phase-shifted periodic distributed structures in optical fibers by UV post-processing', *Electron. Lett.*, 1994, **30**, 1344–5.

30 Tao X M, Tang L Q, Du W C and Choy C L, 'Internal strain measurement by fiber Bragg grating sensors in textile composites', *J. Composite Sci. Technol.*, 2000, **60**(5), 657–69.

31 Tang L Q, Tao X M and Choy C L, 'Measurement effectiveness and optimisation of fibre Bragg grating sensor as embedded strain sensor', *Smart Mater. Struct.*, 1999, **8**, 154–60.

32 Tao X M, 'Integration of fibre optic sensors in smart textile composites – design and fabrication', *J. Text. Inst.*, 2000, **91**, Part 1 No.2.

33 Tang L Q, Tao X M, Du W C and Choy C L, 'Reliability of fibre Bragg grating sensors in textile composites', *J. Composite Interfaces*, 1998, **5**(5), 421–35.

34 Du C W, Tao X M, Tam Y L and Choy C L, 'Fundamentals and applications of optical fiber Bragg grating sensors to textile composites', *J. Composite Struct.*, 1998, **42**(3), 217–30.

35 Rao Y J, 'In-fibre Bragg grating sensors – Measurement and science technology', *Measurement Sci. Technol.*, 1997, **8**, 355–75.

36 Keysey A D, Davis M A, Patrick H J et al., 'Fiber grating sensors', *J. Lightwave Technol.*, 1997, **15**(8), 1442–63.

37 Othonos A and Kalli K, *Fibre Bragg Gratings*: *Fundamentals and Applications in Telecommunications and Sensing*, Artech House, 1999.

38 Volathen M, Geiger H, Cole M J, Laming R L and Dakin J P, 'Low-coherence technique to characterize reflectivity and time delay as a function of wavelength within a long fibre grating', *Electron Lett.*, 1996, **23**(8), 847–9.

39 Volathen M, Geiger H, Cole M J and Dakin J P, 'Measurement of arbitary strain profiles within fibre gratings', *Electron Lett.*, 1996, **23**(11), 1028–9.

40 Volathen M, Geiger H, Cole M J and Dakin J P, 'Distributed grating sensors using low-coherence reflectometry', *J. Lightwave Technol.*, 1997, **15**(11), 2076–82.

11

Hollow fibre membranes for gas separation

PHILIP J. BROWN

11.1 Historical overview of membranes for gas separation

During the last century and a half, the development of membranes has resulted in a voluminous amount of literature on the subject.

One review of membranes by Lonsdale[1] still contained over 400 references, even though the author claimed to have covered only the most relevant references in the article. This review also does not therefore intend to be a comprehensive review of the development of membrane technology; rather it is a short account of the interesting developments that have taken place along with the milestones in 'membranology' that have led to the development of hollow fibres for industrial gas separations.

The development of membrane technology is relatively recent, though membranes have been studied for over 200 years. Some of the early papers were quite outstanding and laid the foundations for today's understanding. In 1829, Thomas Graham[2] inflated water wet bladders containing air by inserting them into a jar filled with CO_2. He explained this effect as being due to the dissolution of the CO_2 in the water in the 'capillary canals' of the membrane, its diffusion through the membrane followed by the release of the CO_2 in the bladder.

J. K. Mitchell in 1831 experimented with the so-called 'penetrativeness' of fluids[3] and investigated the penetration of gases. Mitchell noticed that different gases escaped at different rates from natural rubber balloons and found that there was a 100-fold difference between the rates of escape between carbon monoxide and ammonia. Thomas Graham[4–6] investigated the diffusion of liquids and gases and recognized the potential for separation of gases by mechanical means. The important principles of molecular transport through porous and non-porous membranes were intuitively grasped in these early papers. Thomas Graham's experiments on the molecular mobility of gases were beautifully simple. Graham's diffusiometer as first constructed used

a glass tube 10 inches (25.4 cm) in length and less than 1 inch (2.54 cm) in diameter. The tube was closed at one end with porous plaster of Paris (the plaster of Paris was later replaced by graphite), the tube was filled with hydrogen gas over a mercurial trough, and the graphite plate was covered with gutta percha. On removing the gutta percha, gaseous diffusion took place through the pores in the graphite. Graham had great insight into the mechanism of the diffusional processes, and said that: 'It seems that molecules only can pass; and they may be supposed to pass wholly unimpeded by friction, for the smallest pores in the graphite must be tunnels in magnitude to the ultimate atoms of a gaseous body.' Graham found that the passage times of different gases – H_2, O_2 and carbonic acid – showed a close relation to the reciprocal of the square of the densities of the respective gases. Graham used his diffusiometer not only to study single gases but also to partially separate mixed gases (Graham termed this atmolysis). Graham noted that each gas made its way through the graphite plate independently, each following its own rate of diffusion. Though Graham could be said to be the father of gas separation membranes, it was Fick[7] in 1855, using liquids, who described quantitatively the diffusional process. Fick realized that diffusion was analogous to heat conduction (Fourier's law), and with this hypothesis developed the laws of diffusion. The flux was then defined as shown in Eq. (11.1):

$$J = -AD\frac{\delta c}{\delta x} \qquad [11.1]$$

where c is the concentration, x is the distance, D is the diffusion coefficient, A is the area and J is the flux (one-dimensional). Fick thereafter developed his equational analogy further and obtained Eq. (11.2):

$$\frac{\delta c}{\delta x} = D\left[\frac{\delta^2 c}{\delta x^2} + \frac{1}{A}\frac{\delta A}{\delta x}\frac{\delta c}{\delta x}\right] \qquad [11.2]$$

In order to prove his hypothesis, Fick used two different diffusional-shaped cells containing water and placed a crystalline salt at the bottom of the cells. In case A, the cell was a cylindrical shape and in case B, the cell was a conical shape narrowing at the top.

A steady-state concentration gradient was achieved by changing the water at the top of the vessels. Fick found that, in case A, a linear relationship was observed between the specific gravity of the salt solution and distance down the tube, the gradient giving a measure of the diffusion coefficient. In case B, where the area for diffusion changes with time, he found that the results obtained by experiment compared well with those calculated, thus proving that the laws of diffusion were analogous to those of heat transfer. The calculation for the funnel was done using Eq. (11.2).

11.2   Development of membranes for industrial gas separation

It was, however, a number of decades before the principles laid down by Graham and Fick were to be put into use on a large scale. During the 1940s, uranium was needed for military atomic research and led to a large-scale gas separation membrane system. These membranes were porous and metallic, and were used to separate UF_6 isotopes. Isotope separation had already been achieved by Graham[8] in 1846. Polymers which could withstand the presence of HF were not available in the 1940s. The difference in molecular weight between $^{238}UF_6$ and $^{235}UF_6$ is small and yields a molecular weight ratio of 1.008. The gas mixture was therefore not easy to separate, and thousands of separation stages were needed.

A great breakthrough by Loeb and Sourirajan[9] (reverse osmosis membranes) came about in the early 1960s via the formation of ultrathin membranes of cellulose acetate (CA). These membranes were formed by the casting of a viscous solution of CA and then immersing the cast solution in water. The resulting precipitation gives rise to what is now known as an asymmetric membrane, which consists of a thin dense skin layer which is microporous, supported by a more highly porous sublayer. These thin membranes resulted in high flux and good salt rejection properties. The economic desalination of water was now realizable, and this sparked off a number of studies. Electron microscope[10] studies were carried out in order to determine the thickness of the dense skin layer and mechanisms, and explanations were sought for the formation of these skinned membranes.[11] Calculations as to the effective thickness of the CA membranes were done by Merton, Riley and Lonsdale,[1] and correlated well with those seen from electron microscopy at approximately 0.2 µm.

The adaptation of the principles used in the development of the membranes for the desalination of water via reverse osmosis was all that was needed to develop membranes for gas separation. It was realized that gas separation through dense polymer films was not practicable (due to the low gas flux) unless ultrathin dense films could be obtained. A thin film ensures a high flux even if the intrinsic permeability of the polymer is low. In 1970, using Loeb Sourirajan CA membranes which were dried, Merten and Gantzel[12] obtained a separation factor of approximately 40 for He/N_2, with high fluxes equivalent to those of a silicone rubber film 10 µm thick, but which would have a corresponding separation factor of only 1.5.

But undoubtedly the biggest breakthrough in the last 20 years or so was brought about by the Monsanto Company. Polysulfone, a polymer which at that time was considered to have a high intrinsic selectivity for gases but a low permeability, was utilized in the form of hollow fibres. The Monsanto

PRISM™ system, which used these fibres, was similar to the reverse osmosis system developed by Du Pont, the Permasep RO system. The hollow fibres were asymmetric, with thin skins on the outside supported by a porous layer. The skin in this case was microporous, and the breakthrough was to coat the fibres with a highly permeable polymer which blocked the pores. The separating layer was then the thin dense polysulfone skin layer and not the coating. The resulting fibres have a high flux and high gas separation performance. Henis and Tripodi (the inventors), along with the Monsanto company, issued a series of patents[13–16] in the early 1980s. Following the work of Henis and Tripodi, and with it the reality of commercial membrane systems for gas separation, the 1980s saw a time in which a plethora of work was done in developing the performance of membranes for gas separations. However, the work of Henis and Tripodi is worth describing in some detail since it was undoubtedly their work which caused many researchers to become involved in hollow fibre membranes for gas separations.

The United States Patent 4 230 463 (1980) by Henis and Tripodi describes multicomponent membranes for gas separations. This patent makes 78 claims and contains 7 figures. Sixty-three examples are given in all to demonstrate the flexibility of the invention, its limitations and successful use. A summarized description of the invention is given below.

The multicomponent membrane described in the invention exhibits a separation factor significantly greater than the intrinsic separation factor of the coating material which is used to 'occlude' the pores of a microporous polymer substrate. The intrinsic separation factor of a material is defined as the separation factor of a dry compact membrane of the material. The term 'significantly greater' was defined as being anywhere from 5 to 10% greater than the coating material and preferably 50% higher. The 'occluding contact' refers to the fact that, after coating the membrane, the amount of gas passing through the material of the membrane is increased relative to the amount of gas now passing through the pores. It is claimed that the porous separation membrane could be anisotropic and characterized by having a dense region in a barrier relationship to that of the porous separation membrane. The coating of porous membranes which have a relatively dense skin region provides enhanced flux through the multicomponent membrane. The coatings are applied in a liquid phase (usually a polysiloxane solution in isopentane) and, for advantageous coating, the liquid will adhere to the porous separation membrane to be utilized. It is preferable that the coating material polymerizes after the liquid has been applied to the porous separation material. Suitable porous separation substrates, e.g. polysulfone, cellulose acetate and polyimides, are some of those given. The porous separation membrane is preferably at least partially self-supporting and, with this in mind, hollow fibres were selected. Descriptions of polymer concentrations, the solvents for the spinning

process and the spinning conditions are given in some of the examples in the patent. This patent in itself contains vast amounts of data, as well as a mathematical model (the resistance model), and it paved the way for others containing more detailed examples of spinning conditions and examples of the use of the resistance model. The resistance model was elaborated on by Henis and Tripodi in another paper,[17] and since this model is the basis of Monsanto's work, and since it has been used as a predictor by many other membrane researchers, it is shown below.

11.2.1 The resistance model approach to gas permeation

In the patents and papers which describe the resistance model, it is shown that permeation through composite hollow fibre membranes is analogous to electrical resistance. The symbols used to denote flux or permeation rate are the ones used by Henis and Tripodi. The permeation rate or flux Q_i is given by Eq. (11.3):

$$Q_i = \frac{P_i A \Delta c_i}{l} \qquad [11.3]$$

where P_i is the intrinsic permeability of the polymeric membrane to gas component i, A is the cross-sectional surface area of the membrane to component i, l is the thickness of the membrane area through which the component permeates, and Δc_i is the partial pressure difference across the membrane. The electrical analogy is that the permeation through a polymer membrane is equivalent mathematically to Ohm's law for flow through a resistor, Eq. (11.4):

$$I = E/R \qquad [11.4]$$

The current is analogous to permeation rate, the driving force or voltage is analogous to the concentration gradient or pressure differential, and the electrical resistance is then the analogue of resistance to permeate flow. The resistance to permeate flow can then be said to be R_i:

$$R_i = 1/P_i A \qquad [11.5]$$

Combining Eqs. (11.3) and (11.5), Henis and Tripodi derive Eq. (11.6):

$$Q_i = \Delta c_i / R_i \qquad [11.6]$$

The permeation behaviour of porous hollow fibre membranes is analogous then to the flow of electricity through an array of series–parallel resistors, and the membranes are thus called resistance model or 'RM' composite membranes. A cross-sectional representation of a membrane is shown in Fig. 11.1, along with its electrical analogue. Regions are defined as a skin of thickness l_2 (analogue R_2) defects or pores (analogue R_3), a highly porous substrate
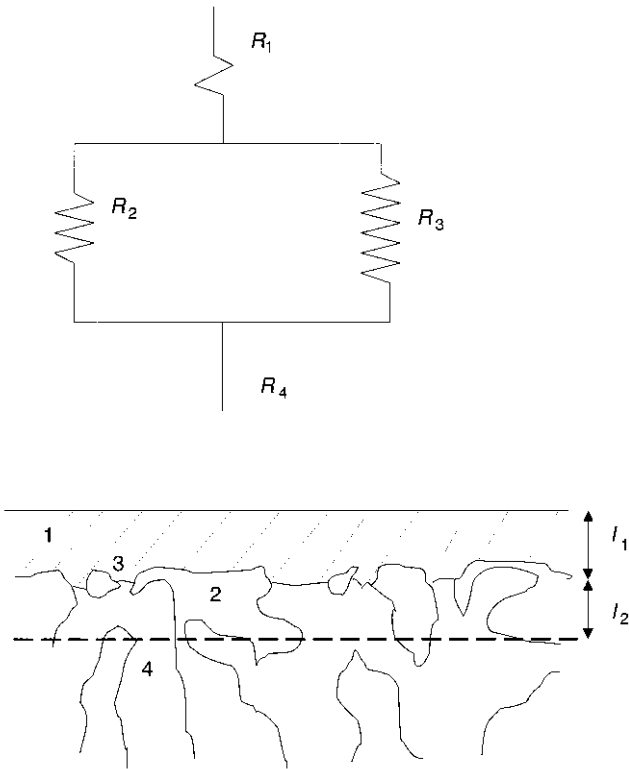
11.1 Representation of a porous asymmetric membrane and its electrical analogue. (From Henis & Tripodi.)

(analogue R_4), and the coating of thickness l_1 (analogue R_1). The total resistance to the flow R_t (see Eq. (11.7)) is a function of the resistance to flow in each of the regions defined within the membrane:

$$R_t = R_1 + \frac{R_2 R_3}{R_2 + R_3} + R_4 \qquad [11.7]$$

The porous substrate resistance R_4 is very small and can be disregarded. The coating R_1 substantially increases the resistance to the passage of gas. The blocked pores resist gas flow one million times more than an open pore. Assuming that the coating layer fills pores to a depth equal to that of the skin layer, the resistance in the pores is given by Eq. (1.8) and the resistance to the coating material is also given:

$$R_{3,i} = \frac{l_2}{P_{1,i} A_3} \text{ and for the coating } R_{1,i} = \frac{l_1}{P_{1,i} A_1} \qquad [11.8]$$
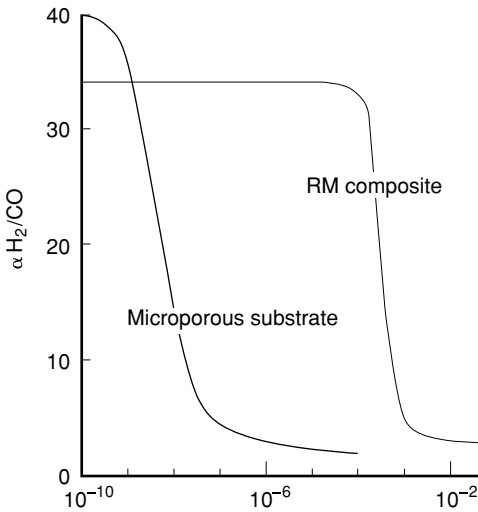
11.2 Effect of surface porosity on separation factor.

The skin resistance is given by Eq. (11.9):

$$R_{2,i} = \frac{l_2}{P_{2,i}A_2} \tag{11.9}$$

The total flux for the composite membrane can be arranged to find the gas flux per unit area and per unit pressure drop, which is equivalent to the thickness corrected permeability or permeation rate (P/l) or P':

$$\left[\frac{P}{l}\right] = \left[\frac{l_1}{P_{1,i}} + \frac{l_2}{P_{2,1} + P_{1,i}(A_3/A_4)}\right]^{-1} \tag{11.10}$$

The surface porosity is low in hollow fibre composite membranes; A_3 is much less than A_2. For simplicity, it can also be assumed then that $A_1 = A_2$.

The separation factor for two gases i and j is the ratio of the (P/l) values (see Eq. (11.11)):

$$\alpha_j^i = \frac{(P/l)_i}{(P/l)_j} \tag{11.11}$$

The effect of the surface porosity on separation factors for H_2/CO for porous substrates and RM composite membranes is shown in Fig. 11.2.

The advantage of the RM composite membrane over a porous substrate membrane is that a far greater variability in the surface porosity of the fibre can be obtained without seriously affecting the flux and separation factor.

Work done by Peinemann et al.[18] uses the resistance model for highly microporous membranes. They showed that the supporting layer in thin film composite membranes can be at least as important as the selective layer. In an extreme case, where N_2 and C_2Cl_4 were separated using a polysulfone–silicone rubber composite, they found that, although the silicone coating was defect free and 87 μm thick, the intrinsic C_2Cl_4/N_2 selectivity of 50 was never obtained. This was due to the high permeability of tetrachloroethylene vapour through the silicone. The non-selective microporous support now resisted the C_2Cl_4 vapour to the same order of magnitude as the silicone layer itself. The Peinemann paper highlights the fact that a non-selective support layer can restrict the flow of a highly permeable gas and reduce separation factors to below those expected.

The Monsanto invention led to the commercial PRISM™ separator.[19] Since the work of the Monsanto team, an international effort has been put into membrane research.

## 11.2.2 Polymer development

Due to the successful implementation of polysulfone in hollow fibre membranes, this system has become the one to outperform. The intrinsic selectivity of polysulfone is high, with a CO_2/CH_4 separation factor of about 29, an H_2/CH_4 separation factor of about 54, and an H_2 permeability of about 10 Barrer. A substantial amount of work has been done in trying to develop new polymers which are more permeable and more selective than polysulfone, while at the same time still tractable. The greatest success appears to have come from the polyimide class of polymers, though others are worthy of note. The work of Koros et al.[20] showed the relationship between the chemical structures in a series of polyimides and their gas separation properties. The polyimides studied are shown in Fig. 11.3.

One of the Koros polymers in particular (6FDA–ODA) exhibited some quite remarkable permeability/separation characteristics. The general rule for a group of polymers such as poly(paraphenylene oxide), polysulfone, polycarbonate and cellulose acetate is that, as the gas selectivity goes up, the permeability goes down. The 6FDA–ODA polyimide does not conform to this general trend. The permeability for 6FDA–ODA to CO_2 at 35 °C at 10 atm was 23 Barrer with a CO_2/CH_4 selectivity of 60.5. This compares to a permeability of 5.7 Barrer and a CO_2/CH_4 selectivity of 27 for polysulfone. The superior performance of the polyimides had shown that, through controlling both the intrasegmental mobility and intrasegmental packing (preferably reducing both), new CO_2/CH_4 could be designed with high permeability and selectivity.

Similar work since by Stern et al. has been done in order to further the
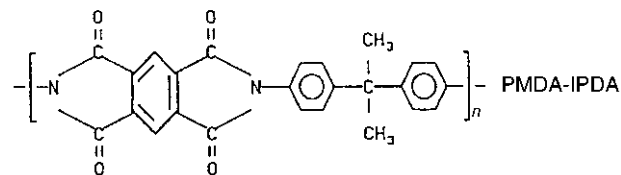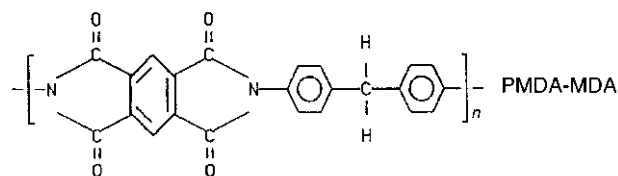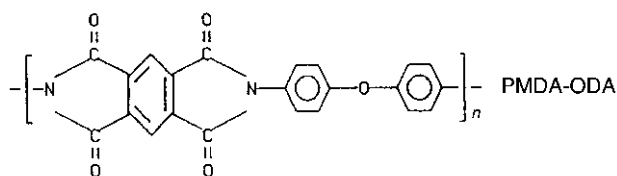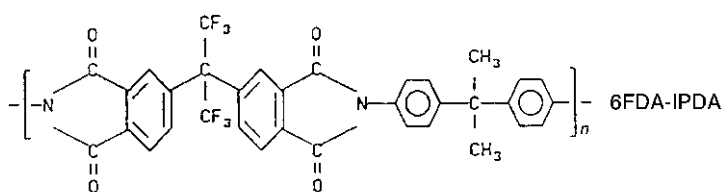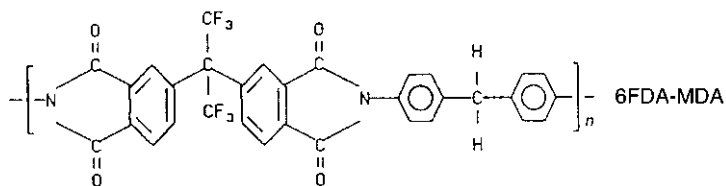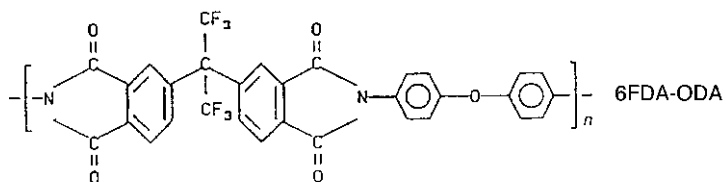
11.3 Polyimides studied by Koros et al.
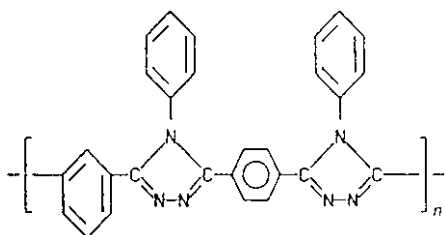
11.4 Poly(1,3phenyl1,4phenyl) 4 phenyl1,3,4triazole.

understanding of the structure property relationships in similar polyimides.[21] Stern used the (6FDA) monomer with a series of diamines to show that relatively small structural modifications of a polyimide can result in large changes in gas permeability. The results from Stern's study are intriguing and, within the polyimide series, the selectivity decreases with increasing permeability, but to a smaller extent than with standard commercial polymers. Stern in discussion points out that anomalies can still occur. For instance, within one polyimide series, the polymer determined to have the smallest interchain spacing and the highest density did not exhibit the lowest permeability and highest selectivity as expected. On the whole, it seems likely that in order to understand the structure/permeability relationships more fully, information on the free volume distribution within the polymer will be required.[22] Smolders et al.[23] worked on developing tailor-made polymers for gas separation. As well as looking at polyimides, they have another polymer (a polytriazole) which was shown to have good permeability and selectivity characteristics. The polytriazole polymer (see Fig. 11.4) has a CO_2 permeability of 10–20 Barrer and a CO_2/CH_4 selectivity of 60.

The polytriazoles are thermally and chemically resistant and are therefore attractive materials for membrane manufacture. The polytriazoles are soluble in formic acid and the polymer can be formed into membranes via a phase inversion technique. One of the problems with the polytriazole is the limited number of solvents available, which in effect reduces the processing flexibility. A slightly different type of membrane but one worthy of note is the ion-exchange type membrane. Here, selective transport of H_2, CO_2 and H_2S has been achieved using facilitated transport gel–ion exchange membranes.[24] The best commercial polymers available achieve an H_2/CO_2 separation factor of around seven to ten, whereas gel–ion exchange membranes can give a much better performance. The ion-exchange membranes in this case are made from polyperfluorosulfonic acid (PFSA) and are modified to form a gel for use as the support for the solvent and carrier. These membranes have hydrophilic regions into which a solvent which has the desired complexing agent is embedded. Typically, H_2O is used as the solvent, with ethylene diamine as the

carrier. Selectivities have been achieved of over 400 for CO_2/H_2, with permeabilities of 11 000 Barrer for CO_2. The high intrinsic permeability is in itself not enough to obtain high productivity for commercial use, as the membrane must also be thin. In one assessment for the economic case for using an immobilized liquid membrane, the film thickness becomes an important economic consideration. Reducing the membrane thickness from 50 μm to 30 μm and increasing the CO_2 permeability from 800 to 2000 Barrer results in a calculated reduction in the required capital investment from \$172 MM to \$12 MM. The difficulty with this type of membrane is to create a mechanically stable gel within a module and to match the properties available from the thick films in the thin ones. If the technical problems can be overcome, facilitated transport membranes will become an economically viable gas separation system.

During the late 1980s, the Japanese C1 chemistry programme put a substantial effort into developing efficient membranes for gas separations. The Japanese budget was approximately £7.5 million on membrane development over 7 years.

The interest of the Japanese lay mainly in the separation of O_2 from air and H_2 from CO. Companies which were interested in hydrogen separation were Ube Industries Ltd., Toyobo Co. Ltd. and Sumitomo Electric Industries Co., whilst those interested in oxygen research were Toyobo, Nitto Electric, Torray, Kururay, Asahi Glass, Teijin and Matsushita Electric. An investigation of porous organic, inorganic and non-porous organic membranes was carried out. The membranes developed during the project exceeded the targets set at the beginning. Materials were evaluated in flat film form and then hollow fibre form. The performance of the various membranes was summed up in a DTI report.[25] Ube developed the polyimide membrane, Sumitomo focused on plasma polymerized membranes, with permeability ratios recorded as high as 300 for H_2/CO, and Toyobo developed a polysulfoneamide membrane and found that increasing the amide content increased the polymer's selectivity. The polyimides made by Ube had better properties than conventional polymers, with a CO_2/CH_4 selectivity of 46, but not as high as those developed by Koros et al., referred to earlier. Reiss et al. achieved a remarkable selectivity using polyaniline polymers.[26] Tailoring the gas selectivity for polyaniline membranes involves doping polymer films with counter ions of an appropriate size. The selectivity reported for H_2/N_2, O_2/N_2 and CO_2/CH_4 surpasses the highest previously reported values of other permeable polymers. Polyaniline $(C_6H_4NH)_n$ was made into a mechanically robust film from a 5% w/v solution in N-methylpyrrolidinone. The cast films were dried in a vacuum for 24 hours and then tested in the 'as cast' form. Samples of the 'as cast' film were doped in 4.0 M acid solution for 15 hours. The films were undoped using 1.0 M NH_4OH for 24 hours. Samples were then redoped by immersion for 12 hours in a 0.0175 M solution of the same acid used in the initial doping, which resulted in

a partially doped film. The effects of the doping and redoping on polymer permeability and selectivity were, to say the least, remarkable. One example of a redoped film gave an incredible separation factor for H_2/N_2 of 3590, with a hydrogen permeability of 10 Barrer. In another example, the dopant cycling procedure achieved a CO_2/CH_4 selectivity of 640, well over 100 times that possible with polysulfone.

However, despite the promise of the polyaniline polymer, its use to manufacture hollow fibre membranes that can compete commercially have so far eluded researchers in the field. This may be due to the difficulties encountered in hollow fibre spinning processes.

11.3   Theories of permeation processes

The permeation of gases through polymer membranes depends upon whether the membrane is porous or dense. If the membrane is porous, the gas flow is predominantly controlled by the mean free path of the gas molecules and the pore size. The mechanism of flow through porous membranes has been discussed elsewhere.[27,28] In short, the gas flow regime is contributed to by Poiseuille flow and Knudsen flow, the amount of each contribution being defined by pore size, pressure, viscosity and the molecular weight of the gas involved. However, microporous membranes exhibit low gas selectivity, as shown earlier in the resistance model approach.

For more efficient separations, dense polymer membranes are used, although they will usually have a high microporous substructure. In dense polymer membranes, gas flow across the membrane is via a solution diffusion mechanism. In simple terms, the gas is sorbed onto the polymer, then diffuses down a concentration gradient via Fick's law (Eq. (11.1)) and finally desorbs from the low pressure side of the membrane. A large number of publications have been written on the subject of the mechanism of gas permeation, and some key arguments have been described elsewhere.[29–40]

11.4   Phase inversion and hollow fibre membrane formation

The term phase inversion refers to the process by which a polymer solution inverts into a three-dimensional network. Initially, the solvent system is the continuous phase, and after phase inversion the polymer is the continuous phase.[41] Four phase inversion processes exist: (1) the dry process, in which a volatile solvent is lost and phase inversion occurs, (2) the wet process, in which solvent is exchanged for non-solvent and precipitation occurs, (3) the thermal process, where a latent solvent (a substance which is only a solvent at elevated temperatures) is used, involving the cooling of the polymer solution which
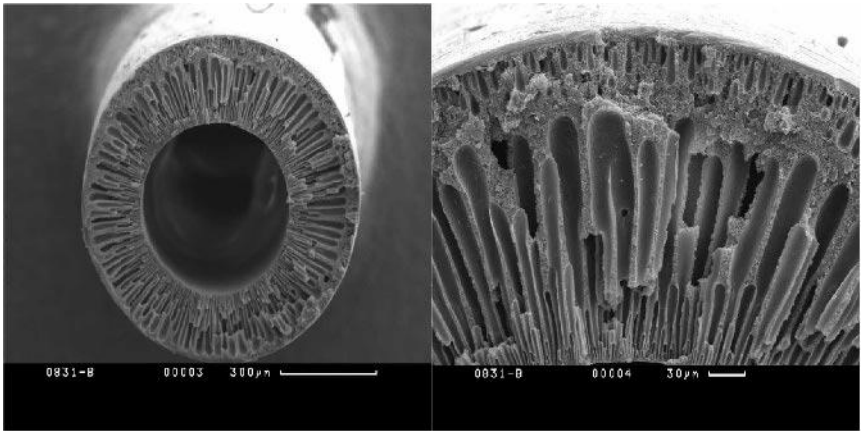
11.5 Finger-type pores in polyetherketone hollow fibres.

then gels, (4) the polymer-assisted phase inversion or PAPI process, where the system contains a solvent and two compatible polymers from which a dense film is cast. The dense film morphology is known as an interpenetrating network, IPN. After complete or partial solvent evaporation from the IPN, the film is usually immersed in water or a solvent which is a solvent for one polymer but not the other.

The hollow fibre membranes reviewed in the present work here are formed using the wet phase inversion process. The wet phase inversion process has been very well described by Strathmann.[42,43] In his work, Strathmann casts various polymer solutions onto glass plates and then immerses the cast film into a bath of precipitation fluid. This kind of precipitation is fast and a skinned membrane structure forms. The skin formation is explained by Strathmann on the basis of the concentration profiles of the polymer, solvent and the precipitant which occurred during the phase inversion process.

In skin-type membranes, like hollow fibre membranes, two characteristic structures can be formed. One structure is sponge-like below the skin, and one has finger-shaped pores below the skin. These finger-shaped pores can be clearly seen in the polyetherketone hollow fibre (see Fig. 11.5).[43,44]

These structures are different when different precipitation conditions are used.[44] The finger-like structures which form cannot be entirely explained by the thermodynamic and kinetic approach. The skin formation is the same as that for sponge-type membranes, but, when the shrinkage stress in the skin cannot be relieved by creep relaxation of the polymer skin, the skin ruptures. The points at which the skin splits form the initiation points for fingers. The exchange of solvent with precipitant in the finger is much faster than through the unfractured skin region. The fingers form a layer of precipitated polymer

around them; the rest of the polymer solution is thus protected from the precipitant and, between the pores, a sponge-like structure is formed. In the case of polysulfone hollow fibre membranes, it was found by Senn[45] that the reduction of these finger-like pores or macrovoids improved the gas separation performance of the fibres. Elimination of macrovoids was achieved by making the appropriate selection of polymer, solvent and precipitant, and then obtaining the correct spinning conditions.

Many investigations have been made to examine the effects of phase inversion on membrane morphology, and the related effects of spinning conditions on hollow fibre membrane morphology and the ensuing gas separation properties. Kesting and Fritzche[46] argue that considering the disadvantages of synthesizing new polymers, namely, increased cost of materials and problems of poorer processing and mechanical properties, better use should be made of commercially available polymers. The work by Monsanto[47] that developed polysulfone second generation hollow fibre membranes justifies this point of view. Thus, the spinning conditions can themselves impact molecular packing, polymer density and interchain displacement to enhance gas separations. The second-generation polysulfone hollow fibre membranes show a fourfold increase in oxygen permeability, with no loss in oxygen/nitrogen selectivity[47] when compared to the original fibres.

The factors affecting membrane structure and performance are many. For example, the better the compatibility between polymer and solvent, i.e. the smaller the solubility parameter disparity between polymer and solvent, the longer it takes to remove solvent from the polymer, therefore the slower the precipitation rate. The greater the precipitant polymer solubility parameter disparity, the faster the precipitation will occur. Increases in the compatibility of polymer and precipitant tend to give membranes with a sponge-type structure (optimum for gas separation), whilst decreasing compatibilities lead to finger-like structures. The solvent precipitant interaction is also important, and a measure of this is the heat of mixing. In systems such as polyetherketone, where the only suitable solvent is 98% sulfuric acid, the heat of mixing solvent and non-solvent (water) is so great that it is difficult to obtain sponge-like membrane structures.[44] However, with polysulfone and polyimides, many types of hollow fibre morphologies can be obtained due to the large numbers of solvents and non-solvent combinations available. Perhaps this is why polysulfone, polyethersulfone and polyimide polymers are still being investigated for their phase separation characteristics.[46–53]

Additives can be added to the precipitant or polymer solution, and these change the activity coefficients for the polymer, solvent or precipitant. In the case of the precipitant, additives such as salts reduce the rate of precipitation and a sponge structure is favoured. In the case of the polymer spinning solution, the same additives generally increase the rate of precipitation and a

finger structure is therefore favoured. Increasing the polymer concentration tends to result in sponge-type structures, whilst low polymer concentrations result in finger-type structures.

The higher the polymer concentration, the higher the strength of the surface precipitated layer, since a higher polymer concentration exists at the point of precipitation and this tends to prevent the initiation of finger pores. Increasing the viscosity of the polymer solution has the same effect. It was shown by Senn[45] that a sponge-type structure was preferable to a finger-like structure, both in terms of permeation rate and separation factor for polysulfone hollow fibre membranes; though some of the early photographs of Monsanto hollow fibres showed the fibres to have finger-type structures, it is unlikely that these fibres are the ones actually used in the PRISM[TM] system.

Moreover, with hollow fibre systems the formation shape and size of the hollow fibre lumen is dependent upon the injection rate and the composition of the internal coagulant, as well as the air-gap in the dry jet wet spinning system. An essential function of the injection fluid is to produce a circular lumen of sufficient diameter to allow the unimpeded flow of the faster permeant gas.

The effects of spinning conditions on fibre morphology and performance have been discussed recently for polyimides,[52,53] polyetherketone[44] and polysulfone. Many papers have been published, examples of which can be found in the following references.[45–51]

11.5   Future hollow fibre membranes and industrial gas separation

Membranes have to compete with the existing gas separation technologies of pressure swing adsorption, cryogenics and absorption. The advantages and disadvantages of each separation technology have been well established.[54]

Within this context, the use of hollow fibre membranes for industrial separation processes has developed, and they can now compete effectively in some cases with conventional processes in terms of energy and capital costs. Membranes for gas separation have developed significantly in the last 20 years; however, there is still a need for high temperature and chemically resistant hollow fibre membranes that exhibit good selectivity and gas permeability. In spite of the developments in gas separation membranes, there are still only a few types of hollow fibre membranes that are commercially available. Polymers currently in use include polysulfone (Monsanto), polycarbonate (Dow Chemical Co.) and polyimide (Medal Co.). Ceramic membranes have found broad application for chemical and temperature resistance, but these are far more expensive and more difficult to make than polymeric membranes.[55]

With this in mind, new better polymeric hollow fibre membranes are still needed that have unique combinations of mechanical toughness, high modulus, thermo-oxidative and hydrolytic stability, resistance to organic solvents and retention of physical properties at very high temperatures up to 250 °C. The challenge continues.

References

1 Lonsdale H K, 'The growth of membrane technology', *J. Memb. Sci.*, 1982, **10**, 81.
2 Hwang S T and Kammermeyer K, '*Membranes In Separations*', John Wiley, New York, 1975 (Prologue by Karl Sollner).
3 Mitchell J K, 'On the penetrativeness of fluids', *Roy. Inst. J.*, 1831, **2**, 101, 307.
4 Graham T, 'A short account of experimental researches on the diffusion of gases through each other, and their separation by mechanical means', *Q. J. Sci.*, 1829, **2**, 74.
5 Graham T, 'On osmotic force', *Phil. Trans.* (The Bakerian lecture), 1854, 177.
6 Graham T, 'On the molecular mobility of gases', *Phil. Trans.*, 1863, 385.
7 Fick A E, 'Ueber diffusion', *Pogg Ann.*, 1855, **94**, 59.
8 Graham T, 'On the motion of gases', *Phil. Trans.*, 1846, 573.
9 Loeb S and Sourirajan S, 'Sea water demineralisation by means of a semipermeable membrane', UCLA Water Resources Centre Report WRCC-34, 1960.
10 Riley R L, Merten U and Gardiner J O, 'Replication electron microscopy of cellullose acetate membranes, *Desalination*, 1966, **1**, 30.
11 Strathmann H and Kock K, 'The formation mechanism of asymmetric membranes', *Desalination*, 1977, **21**, 241.
12 Gantzel P K and Merten U, 'Gas separations with high-flux cellulose acetate membranes', *Ind. Engr. Chem. Process Des. Devel.*, 1970, **9**, 331.
13 Monsanto Co., US Pat 4 230 463, 1980.
14 Monsanto Co., UK Pat 2 100 181 A, 1980.
15 Monsanto Co., US Pat 4 364 759, 1982.
16 Monsanto Co., UK Pat 2 047 162 A, 1980.
17 Henis J M S and Tripodi M K, *J. Memb. Sci.*, 1981, **8**, 233.
18 Peinemann K V, Pinnau I, Wijmans J G, Blume I and Kuroda T, 'Gas separation through composite membranes', *J. Memb. Sci.*, 1988, **37**, 81.
19 Backhouse I, 'Recovery and purification of industrial gases using prism separators' in *Membranes in Gas Separations*, 4 BOC Priestly Conference, Leeds, 1986, 265.
20 Koros W J, Kim T H, Husk G R and O'Brien K C, 'Relationship between gas separation properties and chemical structures in a series of aromatic polyimides, *J. Memb. Sci.*, 1988, **37**, 45.
21 Stern S A, Mi Y and Yamamoto H, 'Structure/permeability relationships of polyimide membranes II, *J. Polym. Sci.*, *Part B*, 1990, **28**, 2291.
22 Private Communication, Dechamps A and Smolders C A.
23 Smolders C A, Mulder M H U and Gebben B, 'Gas separation properties of a thermally stable and chemically resistant polytriazole membrane, *J. Memb. Sci.*, 1989, **46**, 29.
24 Pellegrino J J, Ko M, Nassimbene R and Einert M, 'Gas separation technology',

Proceedings of the International Symposium on Gas Separation Technology, Antwerp, Belgium, 445, 1989.

25 'Modern Japanese membranes', ed. King R, 'Reports from a DTI Sponsored Mission to Japan', 1988.

26 Reiss H, Kaner R B, Mattes B R and Anderson M R, 'Conjugated polymer films for gas separations', *Science*, 1991, **252**, 1412.

27 Hwang S T and Kammermeyer K, *Membranes in Separations*, John Wiley, New York, 1975.

28 Brown P J, 'The modification of polysulphone hollow fibre membranes for gas separation', PhD Thesis, University of Leeds, 1991.

29 Paul D R and Erb A J, *J. Memb. Sci.*, 1981, **8**, 11.

30 Vieth W R, Howell J M and Hsieh J H, 'Dual sorption theory', *J. Memb. Sci.*, 1976, **1**, 177.

31 Petropoulos J H, 'On the dual mode gas transport model for glassy polymers', *J. Polym. Sci. Part B*, 1988, **26**, 1009.

32 Raucher D and Sefcik M D, 'Industrial gas separations', *ACS Symp. Ser. 233*, Amer. Chem. Soc., Washington DC, Chapters 5 and 6, 1983.

33 Datyner A and Pace R J, 'Statistical mechanical model for diffusion of simple penetrants in polymers', *J. Polym. Sci., Part B*, 1979, **17**, 437.

34 Chern R T, Koros W J, Sanders E S, Chen H S and Hopfenburg H B, 'Industrial gas separations', *ACS Symp. Ser. 233*, Amer. Chem. Soc., Washington DC, Chapter 3, 1983.

35 Sefcik M D, 'Dilation of polycarbonate by carbon dioxide', *J. Polym. Sci., Part B*, 1986, **24**, 935.

36 Koros W J and Fleming G K, Comments on measurement of gas-induced polymer dilation by different optical methods, *J. Polym. Sci. Part B*, 1987, **25**, 2033.

37 Meares P, 'The diffusion of gases through polyvinyl acetate', *J. Amer. Chem. Soc.*, 1954, **76**, 3415.

38 Crank J and Park G S, *Diffusion in Polymers*, Academic Press, New York, 1968.

39 Sweeting O J and Bixler H J, *Science and Technology of Polymer Films*, John Wiley, New York, 2 Chapter 1, 1971.

40 Paul D R and Maeda Y, 'Effect of antiplasticization on gas sorption and transport. I. Polysulphone, *J. Polym. Sci. Part B*, 1987, **25**, 957.

41 Kesting R E, *Materials Science of Synthetic Membranes*, ed. Lloyd, Chapter 7, 131, 1984.

42 Strathmann H and Kock K, 'The formation mechanism of phase inversion membranes', *Desalination*, 1977, **21**, 241.

43 Strathmann H, *Materials Science of Synthetic Membranes*, ed. Lloyd, Chapter 8, 165, 1984.

44 Brown P J, Rogers-Gentile V and Ying S, 'Preparation and characterisation of polyetherketone hollow fibre membranes for gas separation', *J. Textile Inst.*, 1999, December 90 Part 3, 30.

45 Senn S C, 'The preparation and characterisation of hollow fibre membranes for gas separation', PhD Thesis, University of Leeds, 1987.

46 Kesting R E and Fritzche A K (eds), *Polymer Gas Separation Membranes*, 2nd edn, John Wiley, New York, 77, 1993.

47 Kesting R E, Fritzche A K, Murphy M K, Cruse C A, Handermann A C and Moore

M D, 'The second-generation polysulfone gas-separation membrane I', *J. Appl. Polym. Sci.*, 1990, **40**, 1557.

48 Brown P J, 'The effect of residual solvent on the gas transport properties of polysulphone hollow fibre membranes', Textile Institute Fibre Science Group Conference, Paper 11, 1989.

49 Brown P J, East G C and McIntyre J E, 'Effect of residual solvent on the gas transport properties of hollow fibre membranes', *Polymer Commun.*, 1989, **31**, 156.

50 Chung T and Hu X, 'Effect of air gap distance on the morphology and thermal properties of polyethersulphone hollow fibres', *J. Appl. Polym. Sci.*, 1997, **66**, 1067.

51 Chung T, Teoh S K, Lau W W and Srinivasan M P, 'Effect of shear stress within the spinneret on hollow fiber membrane morphology and separation performance, *Ind. Eng. Chem. Res.*, 1998, **37**, 3930.

52 Chung T, Xu Z and Huang Y, 'Effect of polyvinylpyrrolidone molecular weights on morphology, oil/water separation, mechanical and thermal properties of poletherimide/polyvinylpyrrolidone hollow fibre membranes, *J. Appl. Polym Sci.*, 1999, **74**, 2220.

53 Wang Dongliang, Li K and Teo K, 'Phase separation in polyetherimide/solvent/nonsolvent systems and membrane formation', *J. Appl. Polym Sci.*, 1999, **71**, 1789.

54 Proceedings of the 4th BOC Priestly Conference, Special Publication 62, Royal Society of Chemistry, 1986.

55 Bhave Ramesh R, *Inorganic Membrane Synthesis, Characteristics, and Applications*, van Nostrand Reinhold, New York, 1991.

12

Embroidery and smart textiles

BÄRBEL SELM, BERNHARD BISCHOFF AND
ROLAND SEIDL

12.1 Introduction

At first glance, embroidery technology seems to have little in common with intelligent textiles and high-tech clothing, since embroidery is generally defined as follows: 'The decoration of woven or knitted textile fabrics or other surfaces, e.g. leather, through the application of threads or other decorative objects (beads, cords, applications), by sewing them in or on in an arrangement designed to achieve a pattern on the ground fabric'.[1]

The 1990s, however, taught us otherwise. Embroidery is the only textile technology in which threads can be arranged in (almost) any direction. The boom in technical textiles has, all of a sudden, created an interest in embroidery technology for mechanical engineering. Arranging high performance fibres, such as Kevlar, carbon fibres, PPS, PBO, etc. in components, according to the lines of force acting upon them, results in elements combining high performance with small mass.

What was until recently unthinkable has now come about: medicine has discovered embroidery. This technology allows wound dressing to be constructed in such a way that embroidered, three-dimensional structures become functional in the healing of wounds.

A combination of aesthetics and innovation is represented in the embroidered stamp, which was introduced as a world novelty in the year 2000 in St. Gallen, Switzerland. Embroidery technology – until very recently used 'just' for decorative purposes – is now slowly penetrating the field of technical textiles. This technology offers unique possibilities and a potential for 'smart textiles'.

12.2 Basics of embroidery technology

Almost all peoples of all regions can look back on a tradition of hand embroidery many centuries old. This was used then, and it still is, for home decorations, clothing, and textiles for cult or religious purposes. The variety of stitches, materials and patterns, which are characteristic features of particular

eras and countries, is huge and beyond visualization. The ground fabric is held in a round frame, the embroiderer pierces the ground fabric by hand with a needle from the top, and the other hand, beneath the embroidery frame, receives the needle, carefully pulls tight the thread and sends the needle to the top again close to the previous stitch. The stitches used include outline embroidery stitches, such as rope, coral, cable, chain or split stitches; flat-mass embroidery stitches, such as couching, satin stitch, darning, cross stitch or appliqué; and shading stitches, such as the feather stitch.

12.2.1 Combined embroidery techniques

Combined embroidery techniques mean that, apart from the ground material and basic embroidery, other additional materials and techniques are used. These products are still categorized as embroidery, even though other techniques such as padding, shearing, etc. are also involved. This is explained by the fact that these are primarily embroidery products. All other techniques are subordinate and merely serve the purpose of the embroidery process, exercising no major influence on the end result.

Combined embroidery techniques without cutwork mean that there are no openings in the ground material. The use of additional materials is frequent with this technique and, less often, other techniques are applied, such as shearing of applications. These combined techniques are divided up into braid embroidery, cord and ribbon embroidery (soutache), appliqués and quilting, and pearl and tinsel embroidery (sequins). The combined embroidery techniques with cutwork comprise thread tensioning and thread pull-out.

12.2.2 Embroidery machines

The fundamental principle of hand embroidery machines is to increase performance by simultaneous operation of a number of needles. Needles with points on either end and eyes in the middle are used. The frame, which holds the ground material, moves to produce a pattern. The needles move in and out of the material along their longitudinal axis. The pattern control is by hand, with a pantograph following an embroidery drawing.

The shuttle embroidery machine is essentially based on the same design as the hand embroidery machine. The most important components of such machines are:

- frame to stretch and move the ground material
  pattern control by hand: pantograph machines
  pattern control by a drive: automatic embroiderer
  electronic pattern control: Positronic

- needle bar with yarn guide
- shuttle bar with drive
- central drive unit.

12.3   Embroidery for technical applications – tailored fibre placement

With the aid of embroidery, through fibre orientation, fibre-composite components can be created to withstand complex forces. This is called tailored fibre placement, TFP.[2]

The process applied is based on embroidery technology, modified to suit the specific technical requirements. A 'cord' of reinforcing fibres is sewn onto the ground material. The arrangement (guiding) of the cord is CNC controlled, and the 'embroidery pattern' is produced with the aid of a computer program. The reproducibility of technical embroidery is good and a change of pattern can be rapidly effected.

The cord can be made of glass, carbon or aramid fibres. Hybrid yarns, consisting of reinforcement and matrix fibres, can also be applied.

A variety of materials can be used as the ground material on which the cord is embroidered, such as woven and non-woven fabrics or foils. In the process, these materials become part of the composite and have to be coordinated with the matrix material. This applies equally to the binding ends, used for the production of the cord. In this way, for instance, glass wovens and polyester ends can be used for a glass/epoxy resin system. For a carbon/PEEK system, PEEK foil and PEEK ends are used. The main advantage, when compared to standard textile technologies, is that reinforcement threads can be arranged in any direction, i.e. at any angle between $0°$ and $360°$. Thus embroidery allows an accumulation of reinforcement material by repeated embroidering across the same place.

To turn the embroidered goods into composites, conventional technologies can be used, such as layout by hand, resin injection processes or pressing. The composite can consist of embroidered products only, or of a combination of standard reinforcement structures.

Examples of typical construction components are:

- rotating machine elements, subjected to centrifugal forces, must be reinforced by radial and tangential structures
- compression-tension bars reinforced by loops and by radial and tangential structures
- levers, subjected to pressure and inflection loads, reinforced by cords, which are arranged along the main stress lines.

12.4   Embroidery technology used for medical textiles

The field of medical textiles is vast. Clothing for hospital staff, surgery blankets, textiles for hygienic and orthopaedic purposes, dressings, implants and much more are included in the wider sense. For future development, products for the healing and construction of human tissue are of particular interest, and this is also the main focus of this chapter. Up to now, products manufactured with embroidery technology have not been available in the medical field. Even though the technique of embroidering has been known for centuries, this field of work has never been touched. However, the first medical products have now been manufactured and are being launched on the market.

For many years, textile structures have been successfully used for wound treatment, operations and implants. The popular range of these products include plasters, wound gauze, dressing material, surgical stitch material, vessel prosthesis and hernia nets. There is a differentiation between external and internal (implant) application. Most products are woven or knitted textile materials, which, for the various applications, are made up according to individual requirements. Figure 12.1 illustrates an embroidered stent.

Today, the use of textile structures in medicine is a growing market. There are constantly new discoveries concerning cellular components, and the reactions of the human body to new and existing substances. New ideas and improvements are needed in order to meet the requirements of this new field.

This is an opportunity for embroidery technology. The process of embroidering allows threads to be arranged on a flat substrate in any direction, thus enabling
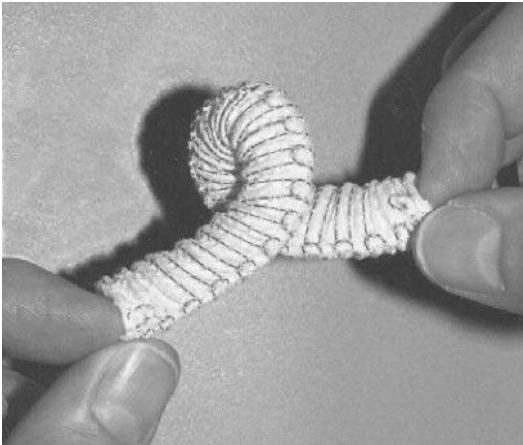
12.1 Embroidery stent, as used for the repair of abdominal aortic aneurysms.

the production of any desirable textile form. This is particularly advantageous with relatively small motifs. As opposed to weaving, where threads are arranged at rigid angles, embroidery also enables rounded patterns. Additionally, made-up embroidery goods are dimensionally stable – unlike knitted fabrics. A further particularity of embroidery is that threads can be placed on top of one another, achieving three-dimensional characteristics. Modern embroidery machines are equipped with colour change devices, enabling switching from one material component to another during the course of production.

Refined and highly sophisticated software enables such flexible production methods. This combines graphics input, of entering images and patterns, with machine language in the embroidery works. The draft of an embroidery pattern is entered into a CAD (computer-aided design) programme, after which it is immediately available for production in machine-readable code. This enables rapid prototyping, so that prototypes to customer requirements can be produced within one day. Ideas from doctors and hospitals can be turned into prototypes equally fast. These rapidly produced embroidered patterns provide a helpful basis for discussion and communication with people from other specialized fields, thus accelerating the development processes.

For medical products, special thread materials are embroidered onto a substrate according to the form required. If a substrate is chosen that is made of polyvinyl alcohol (PVA) or cellulose acetate (CA), it can be dissolved in water or acetone respectively after the embroidery process. The design must ensure that the thread structures hold together securely. Local reinforcements and functional elements can easily be incorporated into the embroidered goods. In an initial phase, the research team with J. G. Ellis[3] has developed embroidered textile implants. They designed hernia patches, implants for intervertebral disc repair and a stent for the repair of abdominal aortic aneurysms (Fig. 12.1). They even used embroidery technology to place and fix rings made of Nitinol shape memory.

In the development of medical textiles, polyester is frequently used. If specialized biocompatible materials are used, they are brought in at a later, more advanced stage of development, due to their high cost (up to 4000 US$/kg). Various synthetic or natural polymer fibres feature very specific structural and mechanical properties, favoured by tissue engineering as bone, cartilage or skin replacements. Karamuk and Mayer[4] carried out tests with embroidered materials that decompose inside the body. These were threads made of polyglycolic acid (PGA). In vitro tests (Fig. 12.2) showed that forces in embroidery goods can be controlled by embroidery technology; in this way, the mechanical properties of the textile can be adapted to those of the body tissue, and inflammatory reactions can be avoided.

The research team, including E. Karamuk,[5] developed a textile wound dressing for the treatment of chronic slow-healing wounds. These embroidered
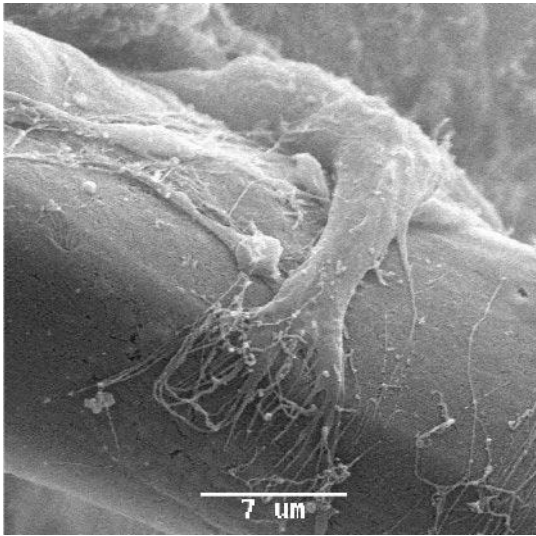
12.2 Cellular growth on a single fibril.
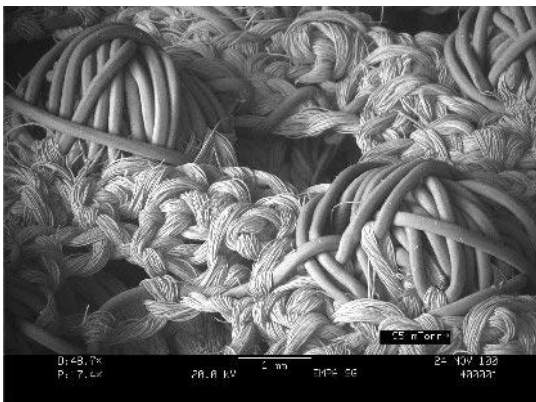
12.3 Electron microscopic view of the embroidered layer of a Tissupor wound dressing.

goods have a three-dimensional structure (Fig. 12.3) and achieve the desired reconstruction of skin tissue. Great attention was paid to the selection of the yarns used: monofilament and multifilament were chosen. In their interstices, multifilaments provide small pores for the body tissue to grow. The spacing between the yarns has larger pores and allows blood vessels to grow into the variously sized holes provided. Apart from the structural configuration of the embroidery goods, stiff elements are incorporated to effect local stimulation of the body tissue. Clinical studies were carried out successfully with patients

who suffered from deep tissue defects due to bedsores, and with patients who suffered from surface wounds due to ulcers caused by bad circulation in their legs.

The growing field of tissue engineering will require more textile structures to support human cells, to reconstruct tissue or entire organs. Possible alternatives, such as transplants or genetic engineering, still leave too many questions unanswered. That is why the means of embroidery technology will yield further products and solutions. Further development work will result in the provision of tailor-made substrates for medical textiles for the healing and regeneration of various wounds and organs.

12.5   Embroidered stamp – gag or innovation?

The world's first embroidered stamp, presented to the public in June 2000, provides further evidence to prove that embroidery technology can be used outside the field of fashion. The agreement on an appropriate size for the forming of proper textile structures was an essential factor. Furthermore, a self-adhesive coating had to be chosen, which would meet the requirements of the post office as well as stamp collectors. Although this project was very successful, it cannot be assumed that embroidery technology will be used as standard technology to produce stamps, since the cost is very high. The limited time available to translate this innovative idea into practice hardly allowed for pure research on the subject. This example demonstrates however that, with flexibility existing technologies can be combined and applied to new areas for
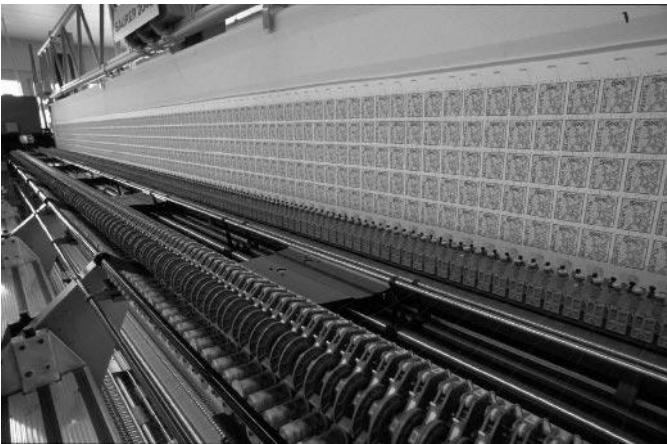
12.4 Production of embroidered stamps on a large embroidery machine.
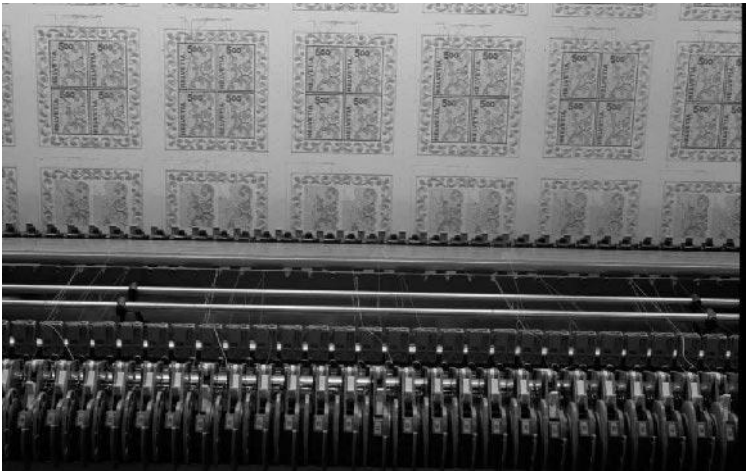
12.5 A square of four stamps on the embroidery machine.

which they were not originally intended. The production of the embroidered stamps on a large embroidery machine is shown in Fig. 12.4 and 12.5.

12.6   Summary

The combination of embroidery technology and intelligent textiles was, until very recently, a contradiction – now they are one and the same. The examples of 'unconventional' uses of embroidery, as presented in this chapter, indicate the potential still to be exploited. However, we are at the very beginning of exploring this field, and extensive research and development work will be required for the eventual manufacture of commercial products. Tailor-made and/or three-dimensional textiles capable of withstanding forces will be with us and clothe us – the smart textiles of the new millennium.

References

1 Seidl R, 'Manuscript of lecture on embroidery', Swiss Textile College, 2000.
2 Seidl R, 'Manuscript of lecture on technical textiles', Swiss Federal Institute of Technology, Zurich, 2000.
3 Ellis J G, 'Embroidery for engineering and surgery', *Textile Institute World Conference*, Manchester (UK), 2000.
4 Karamuk E and Mayer J, 'Embroidery technology for medical textiles and tissue engineering', *Tech. Text. Internat.*, July/August 2000, 9–12.
5 Karamuk E, 'Embroidery technology for medical textiles', *Medical Textiles*, 1999, Bolton, UK.